https://dx.doi.org/10.1016/j.tws.2022.109490

Behavior of GFRP-concrete double tube composite columns

Shuai Li Tak-Ming Chan* Ben Young

Department of Civil and Environmental Engineering, The Hong Kong Polytechnic University, Hong Kong, China

*Corresponding author.

Email address: tak-ming.chan@polyu.edu.hk (T.-M. Chan).

Abstract

A novel glass fiber-reinforced polymer (GFRP) – concrete double tube composite column, which consists of an outer filament winding GFRP tube, an inner pultruded GFRP tube and infilled core concrete and ring concrete, is proposed in this study. A total of 20 specimens were tested to investigate the structural behavior of the composite column. High strength concrete (HSC) was used as the core concrete filled in the inner pultruded GFRP tube, while engineered cementitious composite (ECC) or normal concrete (NC) with medium compressive strength was used as the ring concrete. Different outer and inner GFRP tube thicknesses were considered. Test results reveal that overall performance of the GFRP-concrete double tube composite columns, especially the deformability, is effectively enhanced in comparison to the corresponding normal GFRP-confined HSC columns. Axial load-strain responses and dilation behavior of the composite column were carefully analyzed. Based on the test results, equations are developed to predict the ultimate load carrying capacity and ultimate axial strain for the proposed GFRP-concrete double tube composite column.

Keywords: Composite column, Confinement, Double tube, Load capacity, Pultruded GFRP, Ultimate axial strain

1. Introduction

Composite structural columns are widely used in engineering practices to achieve enhanced performance with the effective utilization of different materials, including concrete, steel and fiber-reinforced polymer (FRP) [1-6]. Various configurations of the composite column section have been developed as shown in Fig. 1. With the confinement provided by steel or FRP tube, concrete is subjected to triaxial compression and could gain improved strength and ductility for concrete filled steel tubular (CFST, Fig. 1(a)) columns [7-8] and concrete filled FRP tubular (CFFT, Fig. 1(b)) columns [9-10]. Extensive analytical models have been proposed to describe the behavior of confined concrete in CFST and CFFT with the consideration of interactions among axial stress and strain as well as lateral dilation and confinement. Among them, stress-path dependent stress-strain model is an advanced analytical model proposed in recent years [11,12]. Stress-path dependence issue of confinement considers the lag between the development of axial strain and that of the confining stress and strain, which is more pronounced with the increase of concrete strength. Modified actively confined concrete model has been proposed to address this effect and could exhibit improved prediction results [13]. Teng et al. [14] proposed the hollow concrete filled tubular sections, which are also termed as double skin tubular columns (DSTCs, Fig. 1(c)) and have been extensively studied through both experimental and numerical investigations over the last decade [15-17]. This structural form presents outstanding economic benefits due to the reduced self-weight. The inner and outer tubes can serve as permanent formwork for concrete casting. FRP tube is normally arranged as the outer tube while steel tube as the inner tube, to achieve the best confinement effect and largest load carrying capacity. Compared with CFFT columns, the ductility performance of DSTCs is significantly improved with the presence of steel tube. Advanced materials, such as ultra-high performance concrete (UHPC), high strength steel and stainless steel, are also used in DSTCs recently to further improve the structural behavior [18-20]. On the basis of DSTCs, double tube tubular columns (DTTCs, Fig. 1(d)) were developed if infilling the inner void with concrete [21-24]. Owing to the dual confinement contributed by outer FRP tube and inner steel tube, the overall performance of the composite column is further enhanced. With the well confined concrete surrounded, inward and outward buckling of steel tube can be effectively restrained and the material strength can be fully utilized. Meanwhile, a residual load bearing capacity will be remained after the rupture of outer FRP tube and can withstand a large axial strain for DTTCs. On the other hand, there are also studies in which the steel tube is arranged as the outer tube, while FRP tube as the inner tube (Fig. 1(e)). It is found that the FRP rupture will be less brittle when embedded in concrete [25]. The outer steel will still provide confinement to the inner crushed concrete and contribute to the axial load capacity under large compressive strains, leading to a gradual failure manner and superior ductility performance [26]. In addition to the section forms composed of circular tubes as presented in Fig. 1, rectangular, square and elliptical steel or FRP tubes are also adopted in composite columns to suit specific engineering applications [22,23,26].

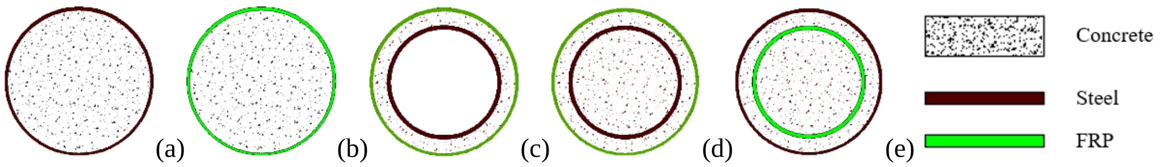

Fig. 1 Configurations of composite columns. (a) CFST; (b) CFFT; (c) DSTC; (d)-(e) DTTC

FRP has the advantages of high strength-to-weight ratio, corrosion resistance and low maintenance cost. Extensive research has been carried out in recent years to investigate the potential of replacing steel with FRP materials, such as FRP rebars and FRP tubes [27-30]. FRP rebars and spirals were used to replace steel rebars and spirals in concrete structures and could realize promising performance under appropriate design guidance [28,30]. Hybrid reinforcing bar, consisting of a central FRP rebar, an external confining FRP tube and high strength cementitious material like UHPC, was proposed by Teng et al. [31] and subsequently investigated under different loading conditions [32]. It was found that the compressive strength of FRP bar could be fully mobilized since both the fiber micro-buckling and FRP buckling were prevented with the support of UHPC. Such steel-free structural members can be used in marine environments to avoid the steel corrosion problem. Meanwhile, seawater sea sand concrete could also be considered to work together with FRP materials for solving the shortage problem of fresh water and river sand in coastal areas [33].

Based on this background, an innovative FRP-concrete double tube composite column is proposed in this study, with the novel section arrangement shown in Fig. 2. It consists of an outer filament winding glass fiber-reinforced polymer (GFRP) tube, an inner pultruded GFRP tube, core concrete filled in the inner tube and ring concrete filled in the region between the inner and outer tubes. Compared with the existing DTTCs, the inner steel tube is replaced with pultruded GFRP tube, as well as two types of concrete can be used in the proposed composite column. There are several advantages that can be achieved for this composite column: (1) with the confinement provided by the outer filament winding GFRP tube, both compressive strength and strain of concrete can be effectively enhanced; (2) the inner GFRP pultruded tube can serve as longitudinal reinforcement, contributing to the axial loading capacity and providing potential bending resistance. With the support of surrounded concrete, compressive strength of pultruded GFRP tube can be fully utilized without premature fiber buckling; (3) different concrete materials can be arranged separately for the core and ring region to obtain improved comprehensive performance; (4) the steel-free column can be used in marine environments without the concern of corrosion problem. Furthermore, seawater sea sand concrete can also be adopted in this proposed composite column. The GFRP-concrete double tube composite column makes full use of the material characteristics of the filament winding and pultruded GFRP tubes. To the best of the authors' knowledge, there has been no research so far that considers a composite column consisting of filament winding FRP tube and pultruded FRP tube simultaneously.

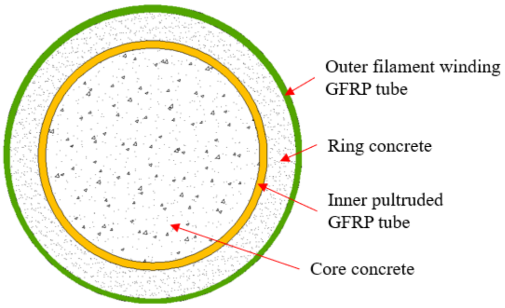

Fig. 2 Section of GFRP-concrete double tube composite column

In this study, a total of 20 specimens were prepared and tested under monotonic axial compression. High strength concrete (HSC) was adopted as the core concrete in the composite column. Different parameters were investigated, including the thickness of outer filament winding GFRP tube, the thickness of inner pultruded GFRP tube and the ring concrete material. Two concrete materials, engineered cementitious composite (ECC) and normal concrete (NC) with medium compressive strength, were arranged separately in the ring region of the composite column. As the fiber-reinforced cementitious material, ECC can develop much larger tensile strength and strain as well as better ductile behavior compared with normal concrete [34-37]. Research on composite structural members with the use of ECC have been emerged in recent years [38-41]. When the HSC core occurs localized cracks due to its brittleness under compression, the NC ring or ECC ring is expected to ease the brittle failure of the column, leading to a more ductile failure. Corresponding GFRP-confined HSC columns were also prepared and tested to make comparison with the proposed GFRP-concrete double tube composite column. Compressive behavior of the pultruded GFRP tube were examined as well through the axial compression tests on hollow pultruded GFRP tubes and HSC filled pultruded GFRP tubes, which also helps to understand the comprehensive behavior of the proposed composite column. Axial load-strain responses and dilation behavior of the composite column were carefully analyzed. Based on the test results, equations are developed to predict the ultimate load carrying capacity and ultimate axial strain for the composite column.

2. Experimental investigations

2.1 Material properties

2.1.1 Concrete

The mix proportions of HSC, NC and ECC adopted in this study are presented in Table. 1. It is noted that 2% volume polyethylene (PE) fiber, with the properties provided in Table 2, was used for the ECC mixture. Five standard cylinders were cast simultaneously when preparing the specimens and were tested to determine the compressive strength and strain for each type of concrete. Compressive properties of HSC, NC and ECC are listed in Table 3. It can be seen that the elastic modulus of ECC is much lower than that of HSC and NC due to the absence of coarse aggregates [35].

Table 1 Concrete mix proportions (kg/m^3)

Concrete	Water	Cement	Fly ash	Sand	Aggregate	S.P.*	Fiber
HSC	120	603	-	693	1023	10.6	-
NC	165	550	-	624	1062	1.5	-
ECC	310.5	554.4	665.2	443.7	-	13.5	19.4

S.P.*: Super plasticizer.

Table 2 Polyethylene (PE) fiber properties

Diameter (μm)	Length (mm)	Density (g/cm^3)	Elastic modulus (GPa)	Tensile strength (MPa)
24	12	0.97	120	3000

Table 3 Concrete material properties

Concrete	Compressive cylinder strength (MPa)	Compressive strain	Elastic modulus (GPa)	Poisson's ratio
HSC	95.1	0.0032	36.8	0.21
NC	63.2	0.0026	32.7	0.22
ECC	55.2	0.0046	15.3	0.21

To examine the tensile behavior of ECC, direct tensile tests were carried out on ECC coupons as per the recommendations of JCSE [42]. Tensile stress-strain curves as well as the specimen failure modes are presented in Fig. 3. ECC coupons exhibited the ductile tensile behavior and multiple fine cracking behavior, with the tensile strength of 5.0 MPa and ultimate tensile strain of 3-4%.

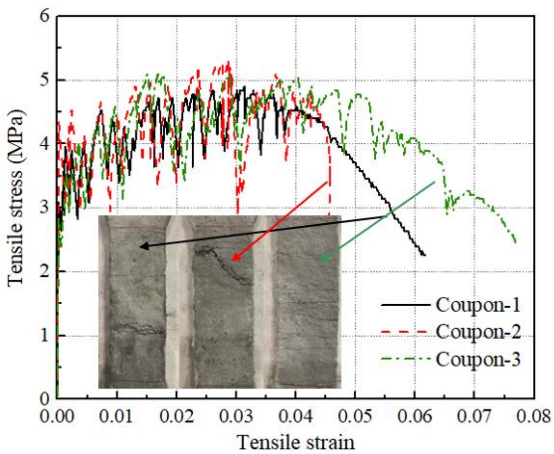

Fig. 3 Tensile behavior of ECC coupons

2.1.2 Filament winding GFRP tube

Outer GFRP tube in the GFRP-concrete double tube composite column was manufactured by filament winding process. It is reported that the compressive strength enhancement ratio of confined concrete can increase substantially with the increase of fiber orientation with respect to the longitudinal direction of the tubes [43,44]. In this study, the fiber orientation was 80 degree to the longitudinal direction to provide confinement to the inner concrete. The nominal inner diameter of the filament winding GFRP tube was 200 mm. Two different tube thicknesses were adopted to provide different levels of confinement and they were 7 layers (F7) and 10 layers (F10) of fiber respectively. Split-disk tests were conducted to obtain the tensile behavior in the hoop direction. Five GFRP rings with the height of 50 mm were cut from the corresponding GFRP tubes and tested as per ASTM D2290-08 standard [45] for F7 and F10, respectively. The results are summarized in Table. 4 and Fig. 4(a). It can be found that the hoop tensile strength, strain and elastic modulus are quite similar for the filament winding GFRP tubes with different thicknesses (F7 and F10). Ring compression tests were carried out to obtain the compressive behavior in the axial direction according to GB/T5350-2005 [46]. The obtained compressive properties as well as typical compressive stress-strain curves are presented in Table 4 and Fig. 4(b).

Table 4 GFRP tube material properties

GFRP tube	Thickness (mm)	Tensile properties			Compressive properties		
		Strength (MPa)	Strain	Elastic modulus (GPa)	Strength (MPa)	Strain	Elastic modulus (GPa)
F7	2.5	620.8	0.0156	39.8	70.6	0.0106	9.5
F10	3.5	630.9	0.0164	38.5	84.6	0.0111	9.7
PF4	4.0	185.5	0.0091	20.4	188.7	0.0114	21.8
PF9	9.0	386.3	0.0103	37.5	379.8	0.0116	35.4

Note: Tensile properties refer to the hoop tensile properties for filament winding GFRP tube (F7 and F10) and axial tensile properties for pultruded GFRP tube (PF4 and PF9). Compressive properties refer to axial compressive properties for both filament winding GFRP tube (F7 and F10) and pultruded GFRP tube (PF4 and PF9).

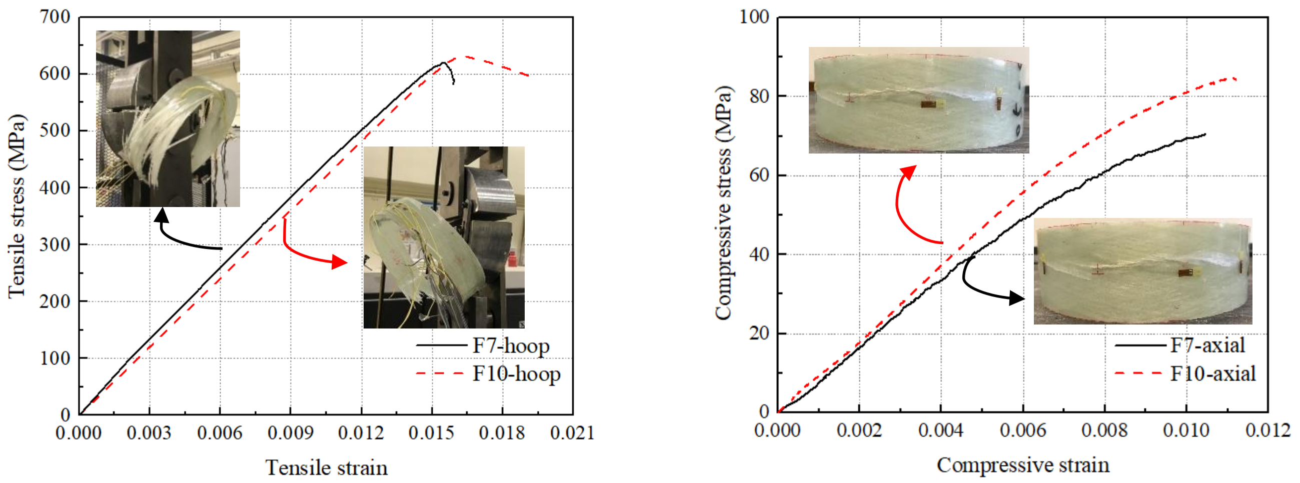

(a) Hoop tensile behavior

(b) Axial compressive behavior

Fig. 4 Tensile and compressive behavior of filament winding GFRP tube

2.1.3 Pultruded GFRP tube

Inner GFRP tube adopted in this study was manufactured by pultrusion process, resulting in a unidirectional fiber matrix architecture. Fiber is distributed along the longitudinal axis of the GFRP tube. Two nominal thicknesses, which are 4.0 mm (for PF4) and 9.0 mm (for PF9), were considered in the double tube composite column. The nominal outer diameter of the pultruded GFRP tube is 150 mm. Five tensile coupon specimens were prepared and tested for PF4 and PF9, respectively. They were cut from the corresponding tubes with respect to the longitudinal axis and prepared as per requirements of ASTM D3039-17 [47], as shown in Figs. 5(a) and (b). The coupons were in the convex and concave shapes for the outer and inner surfaces, since they were cut from the round tube. Slipping or local crushing failure may occur if they are clamped directed to the grips of the testing machine. Therefore, steel plates were attached on the inner and outer surfaces at the two ends with epoxy to form the flat surfaces for solid gripping and contact. Tensile properties of PF4 and PF9 are listed in Table 4, while the typical tensile stress-strain curves are plotted in Fig. 6(a).

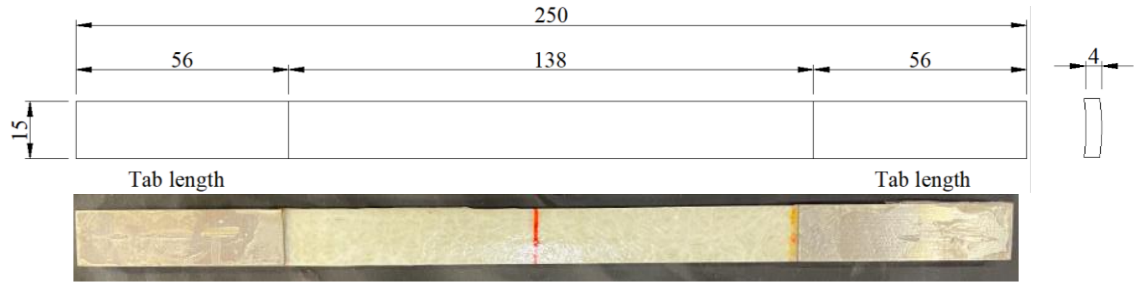

(a) Tensile coupon of FP4 (unit in mm)

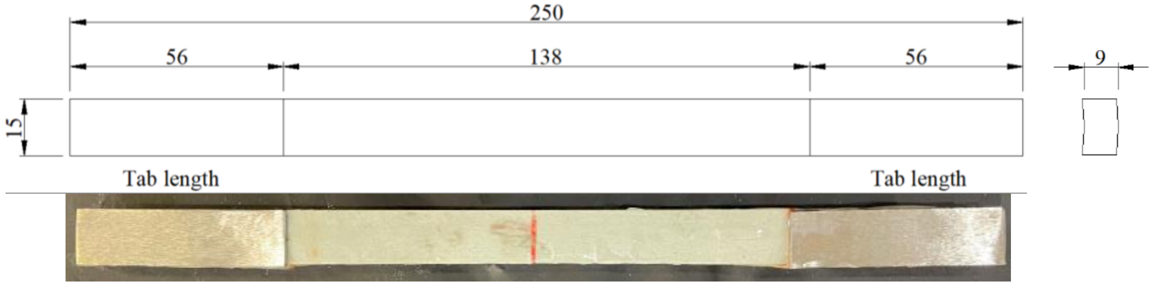

(b) Tension coupon of PF9 (unit in mm)

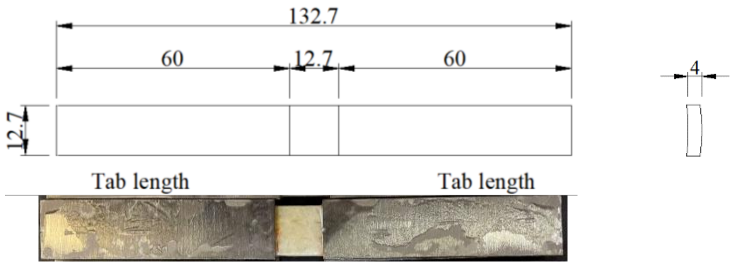

(c) Compression coupon of PF4 (unit in mm)

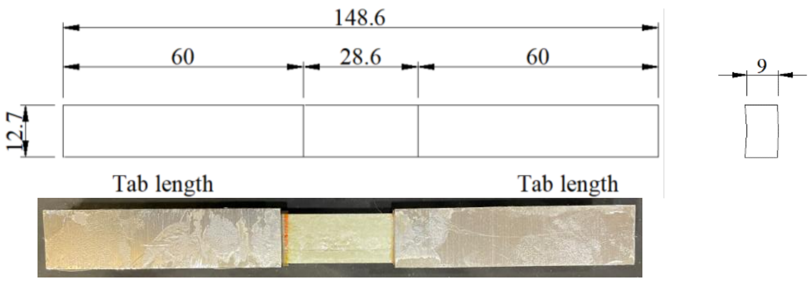

(d) Compression coupon of PF9 (unit in mm)

Fig. 5 Details of pultruded GFRP tube coupons

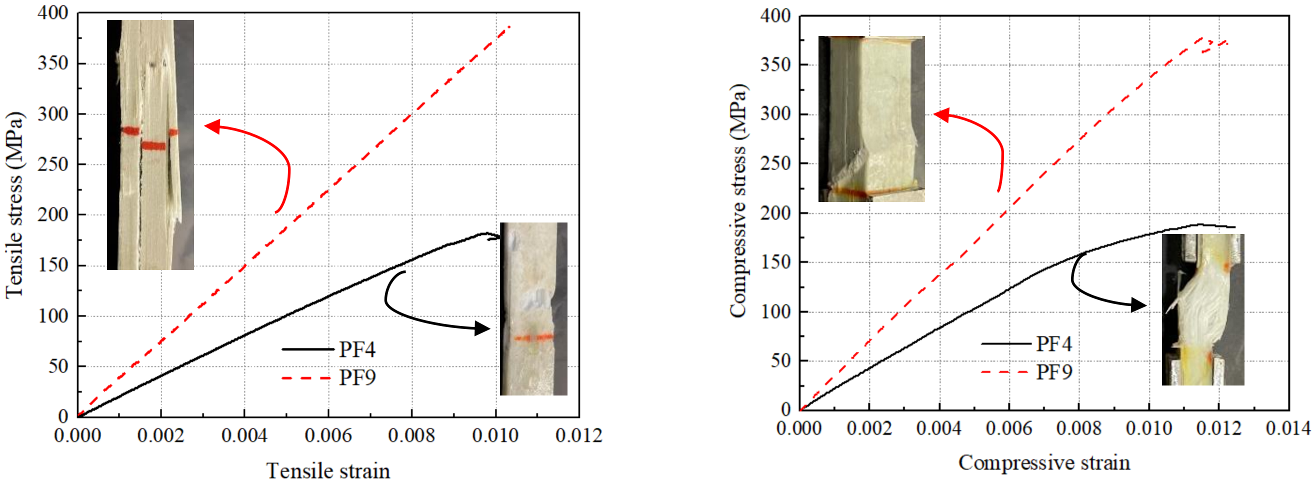

(a) Axial tensile behavior (b) Axial compressive behavior

Fig. 6 Tensile and compressive behavior of pultruded GFRP tube

Compression coupon tests were also carried out to obtain the compressive behavior in the axial direction of pultruded GFRP tubes. Five compression coupons were prepared for PF4 and PF9 respectively in the similar way as tension coupons according to ASTM D695-15 [48] and shown in Figs. 5(c) and (d). Slenderness ratio was carefully checked to avoid global buckling failure. Compressive properties and typical compressive stress-strain curves are presented in Table 4 and Fig. 6(b).

2.2 Test specimens

A total of 12 specimens for GFRP-concrete double tube composite column were prepared and tested under monotonic axial compression. All the specimens had the nominal diameter of 200 mm and nominal height of 400 mm. The height to diameter ratio is 2, which is widely adopted for stub columns to investigate the structural behavior under pure axial compression [14-16,30]. The outer diameter of the inner tube is 150 mm, yielding a 25 mm-thick ring for the composite column. GFRP-confined HSC specimens, hollow pultruded GFRP tubes and HSC filled pultruded GFRP tubes were also prepared and tested in comparison to the double tube composite column. All the specimens are listed in Table 5. For specimen ID, "F" refers to filament winding GFRP tube, while "F7" and "F10" refer to the tubes with 7 and 10 winding layers respectively. "PF" refers to pultruded GFRP tube, with "PF4" and "PF9" representing the nominal thicknesses of the tube are 4.0 mm and 9.0 mm respectively. "H" stands for high strength concrete; "N" stands for normal concrete and "E" stands for engineered cementitious composite. "R" represents the repeated test. For example, "F10-E-PF9-H-R" refers to the repeated specimen of the GFRP-concrete double tube composite column with 10-layer outer filament winding GFRP tube and 9.0 mm-thick inner pultruded GFRP tube, as well as ECC as ring concrete and HSC as core concrete; specimen "F7-H" is a GFRP-confined HSC column with 7-layer filament winding GFRP tube; specimen "PF9-H" is a HSC-filled pultruded GFRP tube with 9.0 mm thickness. Fig. 7 shows the preparation process of double tube specimens. HSC was firstly cast into pultruded GFRP tubes, followed by placing of filament winding GFRP tube outside. Spacers were used at both the top and bottom to guarantee the uniform thickness of the ring throughout the column height. NC or ECC was filled in the ring finally to form the composite column.

Table 5 Key results of the tested specimens

Specimen label	F_1 (kN)	ε_{c1}	F_2 (kN)	ε_{c2}	F_c (kN)	ε_{cu}	F_{max} (kN)	$\varepsilon_{c,max}$	$\varepsilon_{h,rup}$
F7-N-PF4-H	3099.7	0.0107	3065.4	0.0114	3156.9	0.0156	3156.9	0.0156	0.0128
F7-N-PF9-H	3669.1	0.0086	3328.3	0.0119	3385.5	0.0146	3669.1	0.0086	0.0115
F7-E-PF4-H	2535.3	0.0090	2499.7	0.0104	2746.3	0.0155	2746.3	0.0155	0.0113
F7-E-PF4-H-R	2479.7	0.0087	2381.2	0.0098	2827.4	0.0169	2827.4	0.0169	0.0111
F7-E-PF9-H	2968.5	0.0091	2738.3	0.0115	2925.2	0.0155	2968.5	0.0091	0.0092
F7-E-PF9-H-R	3359.4	0.0115	3316.5	0.0144	3442.5	0.0218	3442.5	0.0218	0.0129
F10-N-PF4-H	3458.6	0.0098	3350.4	0.0121	3481.0	0.0160	3481.0	0.0160	0.0120
F10-N-PF9-H*	-	-	-	-	-	-	4371.0	0.0095	0.0072
F10-N-PF9-H-R*	-	-	-	-	-	-	4370.0	0.0105	0.0081
F10-E-PF4-H	-	-	-	-	3229.3	0.0187	3229.3	0.0187	0.0114
F10-E-PF9-H	4185.3	0.0122	3197.4	0.0141	3619.9	0.0199	4185.3	0.0122	0.0109
F10-E-PF9-H-R	4164.5	0.0131	3382.5	0.0146	3592.8	0.0189	4164.5	0.0131	0.0115
F7-H	-	-	-	-	3086.6	0.0118	3365.9	0.0034	0.0110
F7-H-R	-	-	-	-	3093.7	0.0127	3366.8	0.0036	0.0112
F10-H	-	-	-	-	3613.7	0.0135	3613.7	0.0135	0.0121
F10-H-R	-	-	-	-	3729.7	0.0130	3729.7	0.0130	0.0117
PF4	-	-	-	-	-	-	254.0	0.0073	-
PF9	-	-	-	-	-	-	1407.2	0.0102	-
PF4-H	-	-	-	-	-	-	1665.2	0.0031	-
PF9-H	-	-	-	-	-	-	1804.6	0.0033	-

*Note: The specimens F10-N-PF9-H(-R) were not loaded to GFRP rupture due to the capacity limit of the machine. Therefore, 0.0072 and 0.0081 refer to the hoop strains corresponding to F_{max} and $\varepsilon_{c,max}$ for the two specimens, instead of the actual rupture hoop strains.

Fig .7 Preparation process of GFRP-concrete double tube composite columns

2.3 Test setup

Axial compression tests were carried on the MTS 815 rock mechanics system. Test setup and specimen instrumentation are shown in Fig. 8. Twelve strain gauges with the gauge length of 5 mm were attached around the column in the mid height in the hoop direction every 30 degree to monitor the hoop strain distribution. Four strain gauges with the gauge length of 20 mm were attached in the axial direction every 90 degree for axial strain measurement. Four LVDTs were also placed between the top and bottom loading plates to measure the axial shortening of the column. CFRP strips were used to wrap around the column near the two ends for strengthening and to avoid the local failure. Two end surfaces were carefully capped using high strength gypsum material to guarantee the column was in full contact with the loading plates. Monotonic axial compression was applied by displacement control with a loading rate of 0.24 mm/min. All the data, including the axial load and readings of strain gauges and LVDTs, was recorded by a data logger simultaneously.

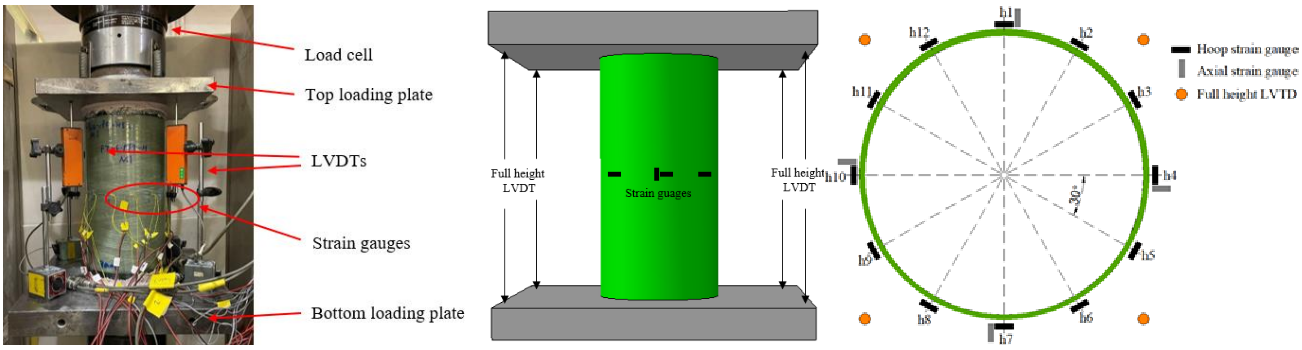

(a) Test setup (b) Instrumentation

Fig. 8 Test setup and instrumentation

3. Test results

3.1 Failure modes

The failed specimens of GFRP-confined HSC column and GFRP-concrete double tube composite column are shown in Fig. 9. All the specimens failed by GFRP rupture on the outer filament winding tube in the hoop direction, as shown in Fig. 9(a). After removing the outer GFRP tube, the cracking and crushing behavior of inner concrete can be observed as shown in Fig. 9(b). Localized diagonal cracks separated the HSC core into two parts from the top to the bottom for GFRP-confined HSC columns (such as the specimen F10-H as shown in Fig. 9(b)), leading to large hoop strains and GFRP rupture at the same locations. For double tube composite columns having ECC as the ring, they would remain as intact with cracks distributed around the ECC surface (such as the specimens F7-E-PF9-H-R and F10-E-PF9-H as shown in Fig. 9(b)). For double tube specimens having NC as the ring, the NC ring would crush and the inner pultruded tube failure could be observed inside (such as the specimens F7-N-PF4-H and F10-N-PF4-H as shown in Fig. 9(b)). Tearing sound could be heard when no rupture failure had been observed on the outer GFRP tube during the test, indicating that the failure of inner pultruded GFRP tube occurred at that moment. Fig. 9(c) shows the splitting failure of the inner tube. It was also observed that the cracking of ECC ring or crushing of NC ring was more obvious at the locations where the inner pultruded GFRP tube failed. Crushing of HSC core in the double tube composite column was also observed and shown in Fig. 9(d).

Failed specimens of hollow pultruded GFRP tube and HSC-filled pultruded GFRP tube are shown in Fig. 10. Buckling was observed for hollow pultruded GFRP tube. Failure of the thicker specimen PF9 was more localized in comparison to that of the thinner specimen PF4, as shown in Figs. 10 (a) and (b). For HSC-filled pultruded GFRP tubes, splitting failure in the hoop direction would occur (as shown in Figs. 10 (c) and (d)) when the HSC core reached the compressive strength, leading to sudden large dilation and concrete crushing.

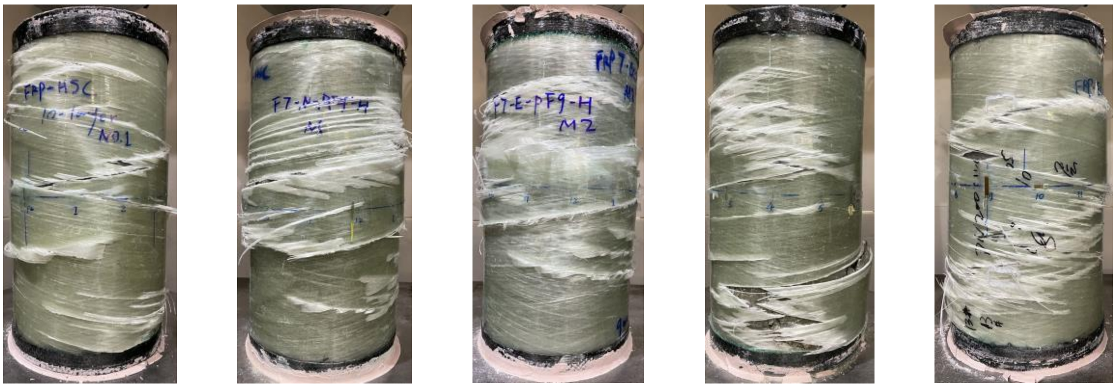

F10-H F7-N-PF4-H F7-E-PF9-H-R F7-N-PF9-H F10-E-PF9-H

(a) Rupture of outer filament winding GFRP tube

F10-H F7-N-PF4-H F7-E-PF9-H-R F7-N-PF9-H F10-E-PF9-H

(b) Cracking and crushing of concrete

(c) Splitting failure of inner pultruded GFRP tube

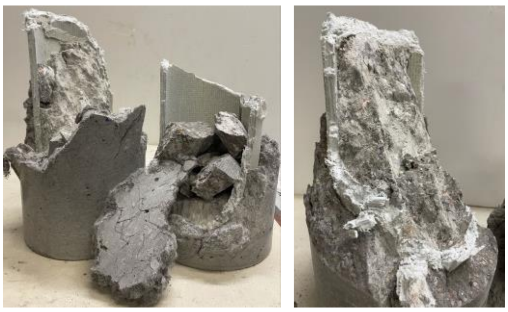

(d) Crushing of HSC core

Fig. 9 Typical failure modes of GFRP-confined HSC column and GFRP-concrete double tube composite column

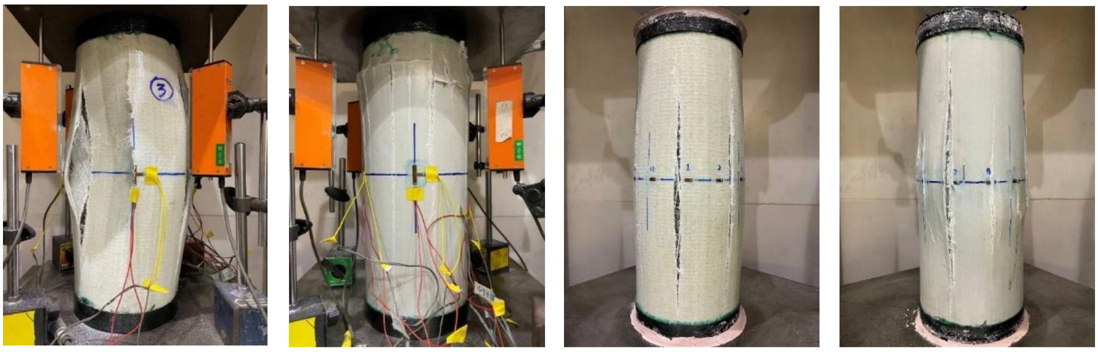

(a) PF4 (b) PF9 (c) PF4-H (d) PF9-H

Fig. 10 Failure modes of hollow pultruded GFRP tube and HSC-filled pultruded GFRP tube

3.2 Axial load-axial strain responses

Axial load-axial strain curves of the tested specimens are plotted in Fig. 11. It is noted that the axial strain can be determined by axial strain gauges as well as by the full height LVDTs as shown in Fig. 8. The readings of the four axial strain gauges were nearly the same at the initial loading stage, indicating the application of pure axial compression without eccentricity. However, with the increase of the loading, the readings of the four strain gauges deviated with each other. This behavior is also reported in literature [49] and is believed to be caused by the non-uniform damage and cracking of inner concrete. On the other hand, the readings of the four LVDTs, which represented the axial shortening of the column, were almost the same during the whole loading process. Meanwhile, axial strain calculated by the LVDTs were close to that recorded by the strain gauges at the initial stage. Therefore, axial strain is determined with the average reading of the four LVDTs and the corresponding column height in this study for analysis and discussion.

Axial load-axial strain curves of GFRP-confined HSC columns are shown in Figs. 11(a) and (b). For specimens F7-H and F7-H-R, there was a significant load drop after the first peak point, followed by load recovery until GFRP rupture. However, the ultimate axial load was still lower than the load corresponding to the first peak point. With the outer GFRP tube thickness increased, the ultimate load was higher than the first peak load for specimens F10-H and F10-H-R, indicating an effective confinement on the HSC core was achieved. For GFRP-concrete double tube composite columns as shown in Figs. 11(c)-(j), all the specimens would have the enhanced loading capacity. Meanwhile, the ultimate axial strains were obviously improved in comparison to the corresponding GFRP-confined HSC columns, demonstrating the good deformability of the newly proposed composite column. The load-strain curves for GFRP-concrete double tube composite columns present different feature compared with those for GFRP-confined HSC columns. The behavior will be discussed in detail in section 4.1 with illustrations of the characteristics of the different components in the composite column. Linear load-strain relationships can be observed in Fig. 11(k) for hollow pultruded GFRP tubes under axial compression until failure. Compared with PF4, both the load capacity and compressive strain were higher for PF9. With the infilled of HSC into the pultruded GFRP tubes, PF4-H and PF9-H failed at the similar axial strain which was corresponding to the HSC core crushing (Fig. 11(l)). PF4-H would lose the capacity completely, while PF9-H would maintain about half of the maximum capacity after the HSC core failure, then followed by the load decreasing gradually.

It should be noted that the loading was suspended for specimens F10-N-PF9-H and F10-N-PF9-H-R when the axial load achieved the actual maximum loading capacity of the machine (which is around 4370 kN) as shown in Fig. 11(h). Therefore, both two specimens were not failed with rupture of the outer GFRP tube.

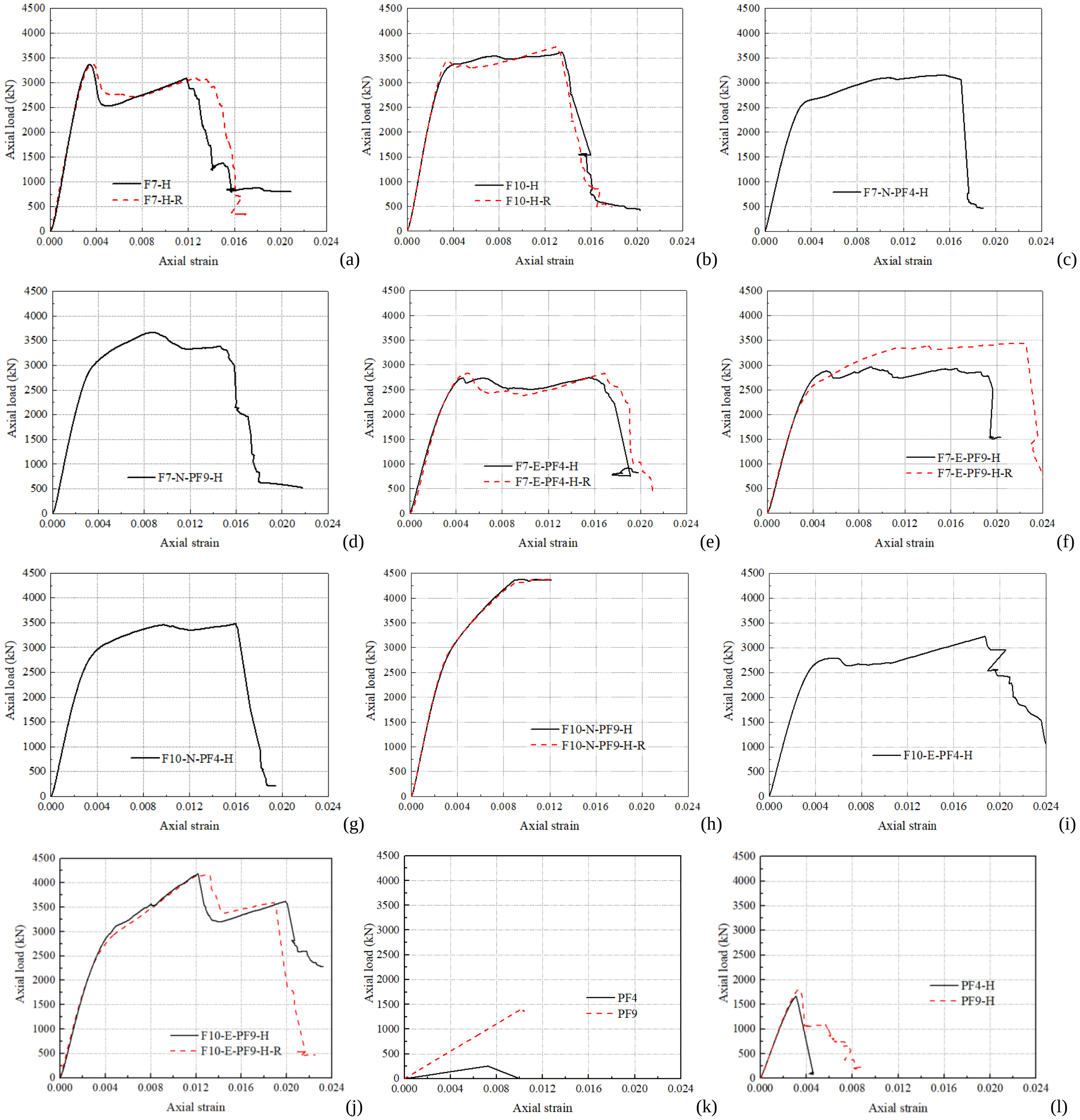

Fig. 11 Axial load-axial strain curves for tested specimens

3.3 Hoop strain-axial strain responses

Hoop strain on the outer filament winding GFRP tube reflects the dilation behavior of the column and the confinement effect applied on the inner concrete. It also governs the failure of the column when the hoop strain reaches the ultimate tensile strain of the filament winding GFRP tube. Hoop strain was calculated by averaging the readings of the twelve hoop strain gauges and was plotted against axial strain before GFRP rupture for GFRP-confined HSC columns and GFRP-concrete double tube composite columns in Fig. 12. It is noted that negative values were assigned to hoop strains, while positive values were assigned to axial strains. The average hoop strains at GFRP rupture $\varepsilon_{h,rup}$, which is also the hoop strain corresponding to the ultimate axial strain ε_{cu}, are listed in Table 5 for all the tested specimens.

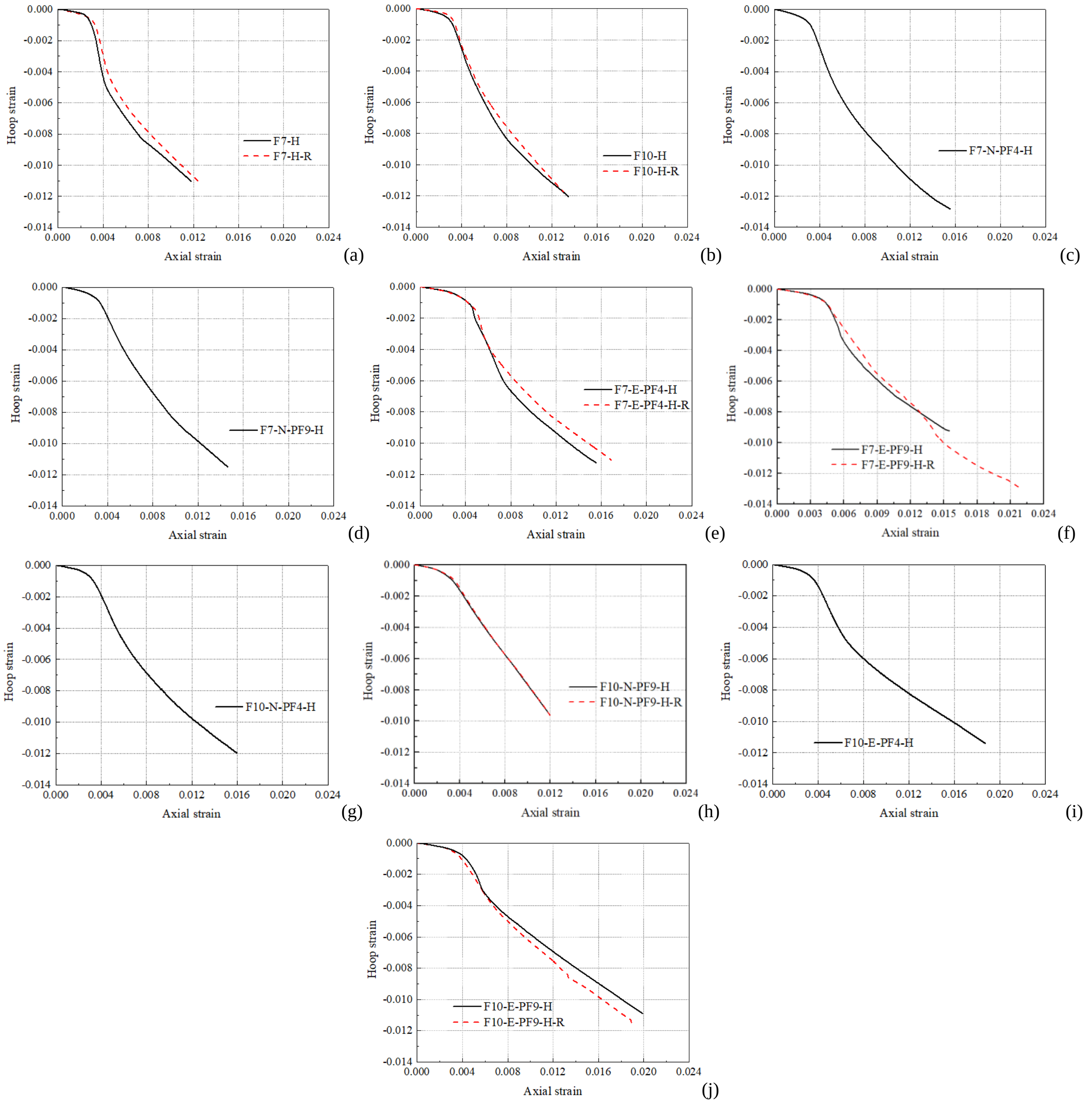

Fig. 12 Hoop strain-axial strain curves for tested specimens

4. Discussions

4.1 Compressive behavior analysis

Fig. 13 shows the compressive stress-strain curves for different components in the GFRP-concrete double tube composite column. It is noted that the curves for filament winding GFRP tube, HSC, NC and ECC are based on the compressive material tests of F7 ring, HSC cylinder, NC cylinder and ECC cylinder, while the curve for pultruded GFRP tube is calculated from the axial load-strain curve of PF9 as shown in Fig. 11(k) with the corresponding cross-sectional area. Due to the hoop fiber orientation, filament winding GFRP tube is weak in the axial direction with low elastic modulus. For pultruded GFRP tube and concrete materials (ie. HSC, NC and ECC), they will fail at different compressive strength and strain. Compared with HSC and NC, the pultruded GFRP tube has much larger failure compressive strength and strain. Compared with HSC and NC, ECC has a larger failure compressive strain with a lower elastic modulus. Therefore, the different components in the composite column will not fail simultaneously when they are compressed under the same axial strain.

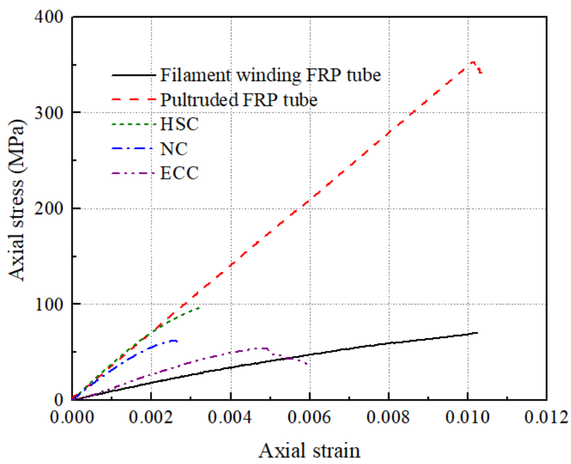

Fig. 13 Axial stress-strain curves for different components in the composite column

Hoop strain-axial strain curves, which reflect the lateral dilation property under axial compression, are shown in Fig. 14 for different components in the double tube composite column. For filament winding GFRP tube, the fiber orientation is 80 degree with respect to the longitudinal direction. It leads to a much larger stiffness in the hoop direction than that in the axial direction. The lateral dilation increases more slowly than pultruded GFRP tube, which has all the fiber oriented in the axial direction and as a result low stiffness in the hoop direction. The calculated Poisson’s ratios for filament winding GFRP tube and pultruded GFRP tube are 0.11 and 0.35, respectively. Therefore, the hoop strain for filament winding GFRP tube is lower than that for pultruded GFRP tube under the same axial strain. For HSC, NC and ECC, the hoop strain increases linearly with the increase of axial strain in the initial elastic stage, with the similar Poisson’s ratio 0.20. Non-linear behavior occurs with the hoop strain increasing much faster due to the development of concrete damage and cracking after the elastic stage. For plain HSC, NC and ECC, they will fail suddenly when the compressive strengths are reached. It is worth noting that the Poisson’s ratio of filament winding GFRP tube is lower than that of the concrete materials, indicating that the confining GFRP tube can get contact with and provide confinement to the confined concrete during the whole loading process.

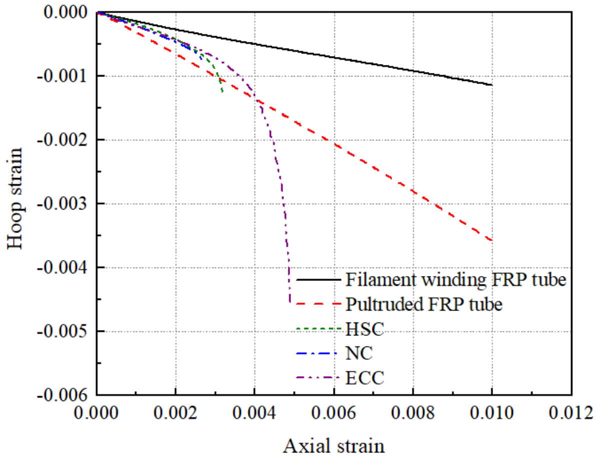

Fig. 14 Hoop strain-axial strain curves for different components in the composite column

With the clear illustrations of axial stress-strain behavior and dilation behavior for the different components, the compressive behavior of the GFRP-concrete double tube composite column could be analyzed and understood more comprehensively. Typical axial load-axial strain curve and hoop strain-axial strain curve for the double tube composite column under axial compression are shown in Fig. 15. In the initial stage OA, hoop strain increases slowly and limited confinement is triggered. After the transition point A, concrete starts to dilate much more quickly due to the cracking behavior as illustrated in Fig. 14, leading to the faster development of hoop strain for the composite column as shown in Fig. 15. Meanwhile, effectively GFRP confinement is provided as well and leads to the strain hardening stage.

At point B with the axial load F_1 and the corresponding axial strain ε_{c1}, it can be noted there is a significant load drop. It is caused by the failure of the inner pultruded GFRP tube. It is worth noting that the axial strain ε_{c1} of the GFRP-concrete double tube composite column could be larger than the failure strain of the hollow pultruded GFRP tube under compression as shown in Fig. 13. This is because that the core concrete and ring concrete, which are both under effective confinement, could provide restrain to the pultruded GFRP tube and thus delay the failure. Meanwhile, the load drop between points B and C is smaller than the load capacity of the corresponding pultruded GFRP tube, indicating that there is still residual capacity contributed by the pultruded GFRP tube in the double tube composite column.

Since the outer filament finding GFRP tube is still providing the confinement to the inner concrete, axial load starts to recover at point C (ε_{c2}, F_2). The second strain hardening stage will end at point D (ε_{cu}, F_c) when the ultimate hoop tensile strain is reached for the outer filament winding GFRP tube, followed by column failure.

It should be noted that the ultimate load capacity F_c at point D could be either higher or lower than the load capacity F_1 at point B. For example, the specimen F10-E-PF9-H has relatively large load drop in stage BC. The second strain hardening stage CD is not long enough for the axial load to recover to the value before the drop. For the specimen F7-N-PF4-H, on the contrary, the load dropped in stage BC is less significant compared with the load gained in the second strain hardening stage CD. Maximum load capacity F_{max} is taken as the larger one between F_1 and F_c and summarized in Table 5, with $\varepsilon_{c,max}$ referring to the corresponding axial strain. The axial loads and corresponding axial strains at points B, C and D are also listed in Table 5.

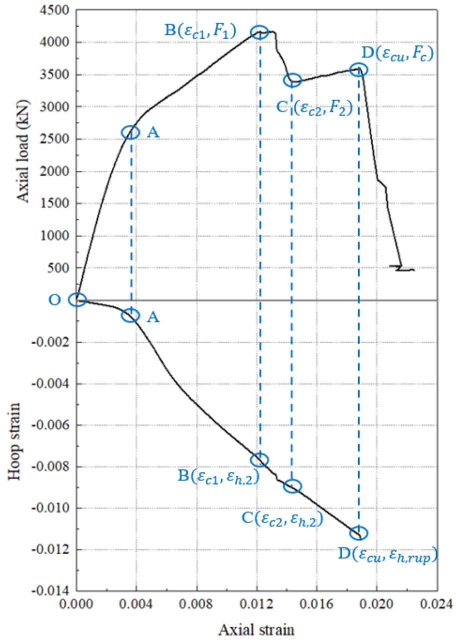

Fig. 15 Typical compressive behavior of GFRP-concrete double tube composite column

4.2 Hoop strain distributions

Hoop strain is of vital importance for the investigation of confinement behavior for GFRP-confined concrete. With the use of the twelve strain gauges attached on the surface of the outer filament winding GFRP tube, hoop strain distribution can be measured and plotted in Fig. 16 for each specimen. It can be observed that the GFRP-concrete double tube composite columns (as shown in Figs. 16(e-p)) could generally achieve a more uniform hoop strain distribution in comparison to the corresponding GFRP-confined HSC columns (as shown in Figs. 16(a-d)). It is widely accepted that concrete cracking pattens can have large influence on the hoop strain behavior [50-53]. Fig. 17 shows the diagram of failure mechanism for GFRP-confined HSC and GFRP-concrete double tube composite columns under axial compression, in conjunction with the comparisons of failure modes of tested specimens. Due to the brittle characteristic, HSC can develop localized cracks under compression, which will lead to highly concentrated hoop strains at the corresponding locations on GFRP tube for GFRP-confined HSC columns as shown in Fig. 17(a). With the presence of the inner pultruded GFRP tube, the HSC core is separated from the NC/ECC ring, so that the concentrated hoop strain cannot be spread out directly for GFRP-concrete double tube composite columns as shown in Fig. 17(b). The ring concrete is less brittle with the relatively lower compressive strength. Therefore, more dispersed cracks can generate in the ring concrete, leading to a more uniform hoop strain distribution on the outer filament winding GFRP tube.

Meanwhile, it can be observed in Fig. 16 that the hoop strain distribution is more uniform for specimens with PF9 as inner tube (as shown in Figs. 16(f,i,j,l,m,o,p)) compared with the specimens with PF4 as inner tube (as shown in Figs. 16(e,g,h,k,n)), since this hindering effect could be more obvious for the specimens with thicker inner tube. Compared with the specimens with NC as ring concrete (as shown in Figs. 16(e,f,k-m)), the specimens with ECC as ring concrete (as shown in Figs. 16 (g-j,n-p)) can exhibit even more uniform hoop strain distribution. It is believed that the ECC ring could help to redistribute the hoop strain due to the good tensile and multiple cracking behavior and further avoid the strain concentration.

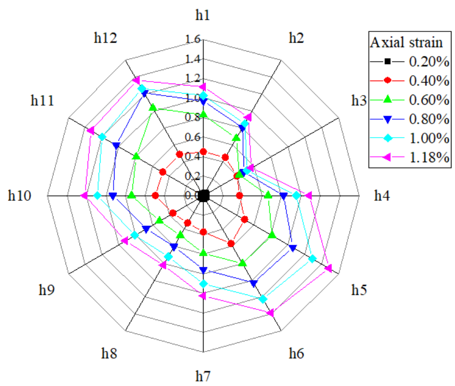

(a) F7-H

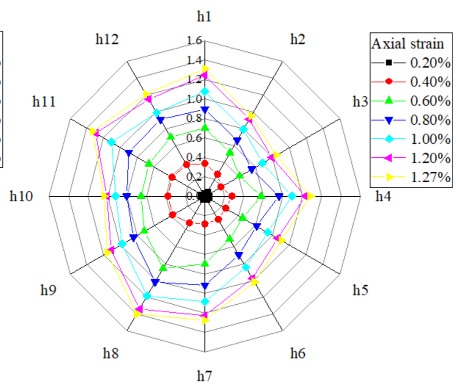

(b) F7-H-R

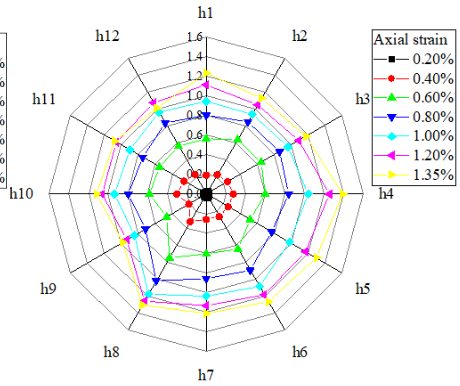

(c) F10-H

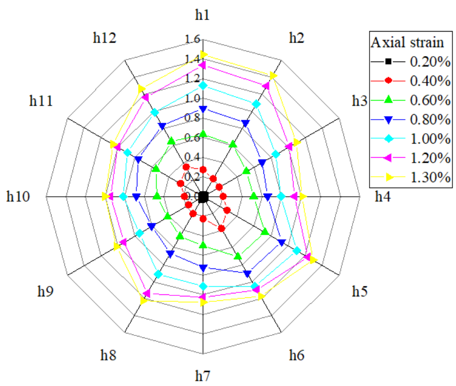

(d) F10-H-R

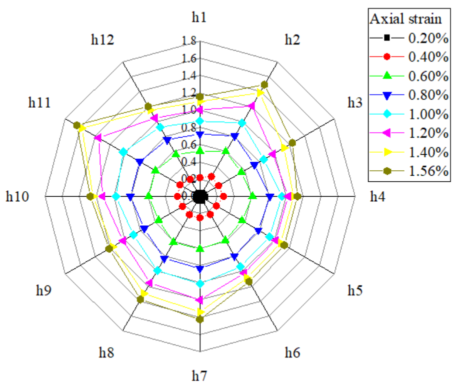

(e) F7-N-PF4-H

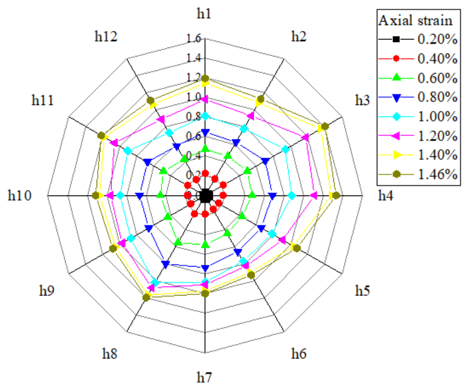

(f) F7-N-PF9-H

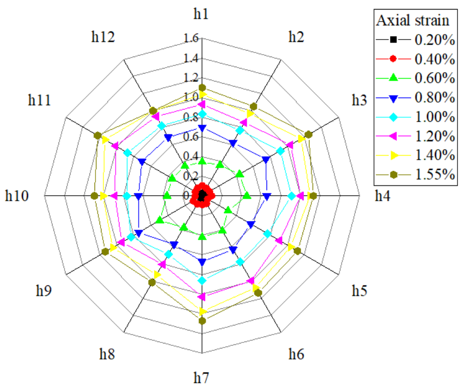

(g) F7-E-PF4-H

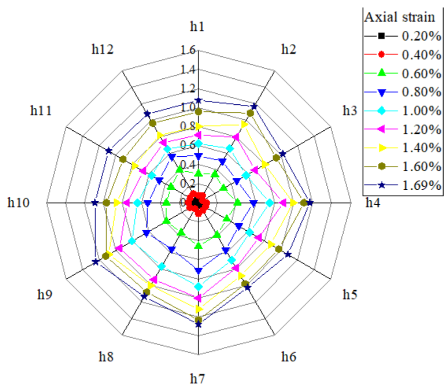

(h) F7-E-PF4-H-R

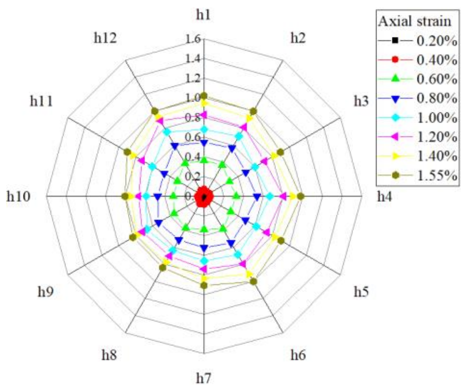

(i) F7-E-PF9-H

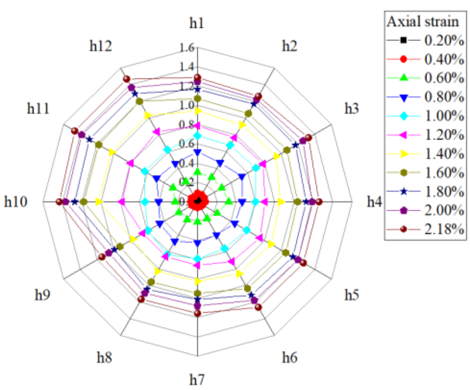

(j) F7-E-PF9-H-R

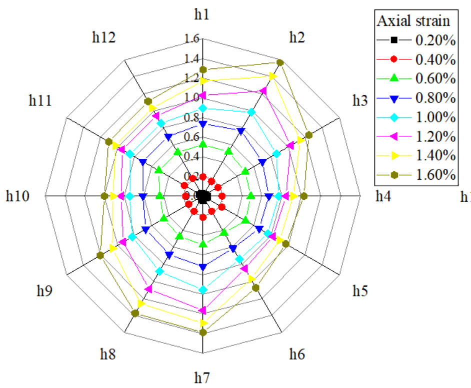

(k) F10-N-PF4-H

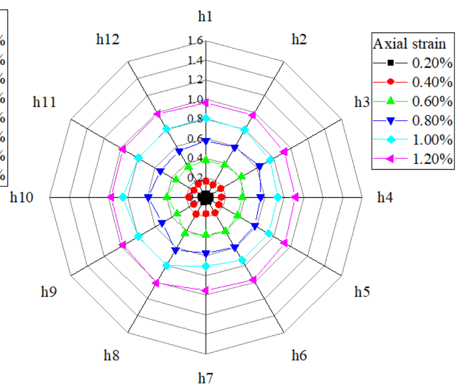

(l) F10-N-PF9-H

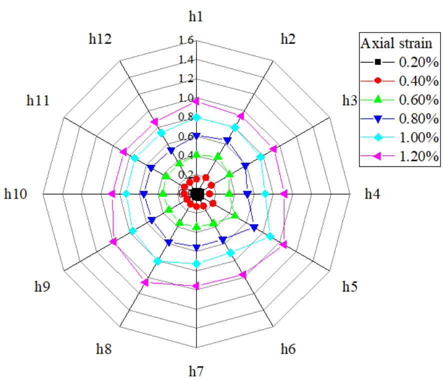

(m) F10-N-PF9-H-R

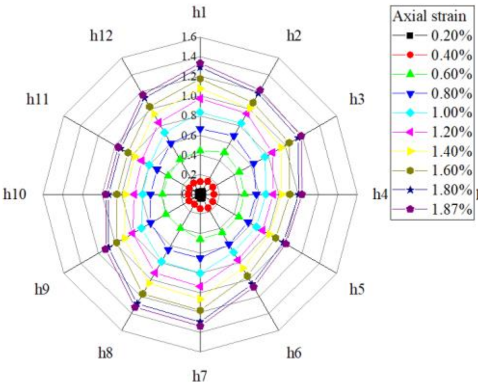

(n) F10-E-PF4-H

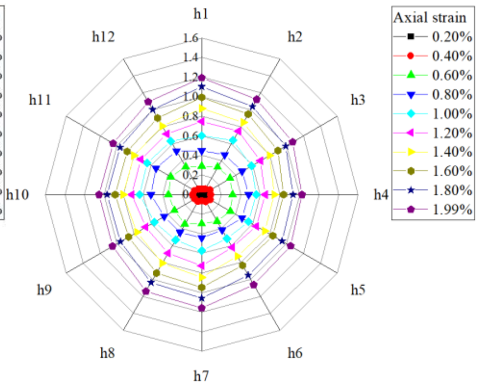

(o) F10-E-PF9-H

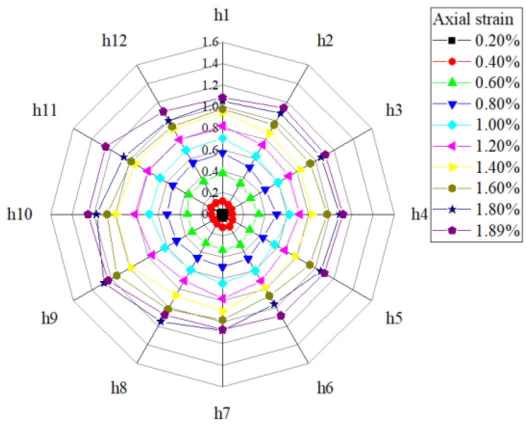

(p) F10-E-PF9-H-R

Fig. 16 Hoop strain distribution of tested specimens

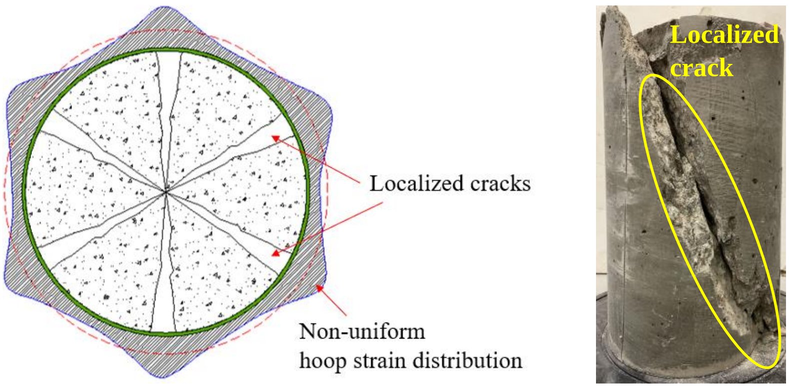

(a) GFRP-confined HSC column

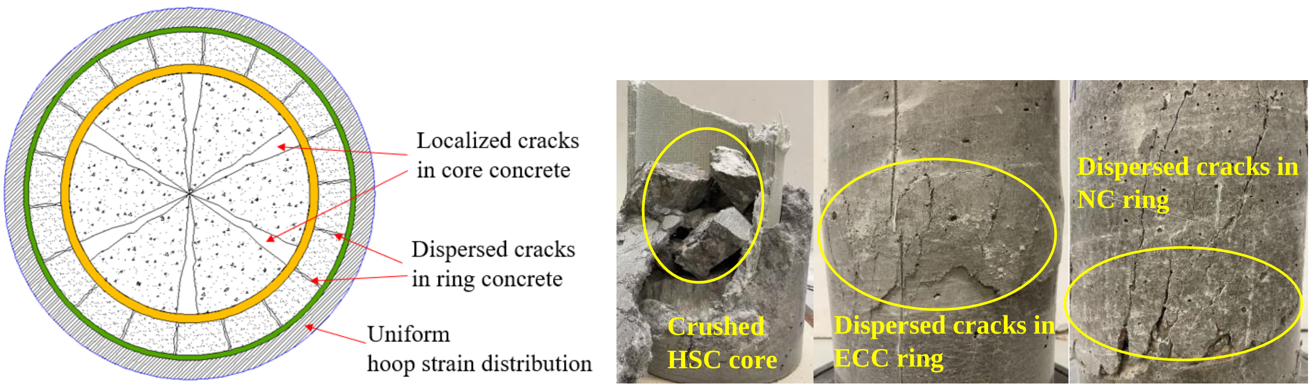

(b) GFRP-concrete double tube composite column

Fig. 17 Failure mechanisms for GFRP-confined HSC column and GFRP-concrete double tube composite column

4.3 Effects of different parameters

4.3.1 Filament winding GFRP tube thickness

The comparisons of axial load-strain response for specimens with different outer filament winding GFRP tube thicknesses are presented in Fig. 18. With the increase of outer GFRP tube thickness, the confining stiffness is increased. For GFRP-confined HSC columns, the load drop after the first peak is eliminated when using thicker outer GFRP tube F10. Both the ultimate load capacity and ultimate axial strain is improved accordingly. For GFRP-concrete double tube composite columns with PF4 as inner tube, the observed axial load-axial strain curves for specimens with different outer GFRP tube thicknesses are similar as shown in Figs. 18 (b) and (d). For double tube columns with PF9 as inner tube, larger stiffness of the strain hardening stage can be noted for the specimens with the thicker outer tube F10 as shown in Figs. 18(c) and (e). Hoop strain-axial strain curves for specimens with different outer filament winding FRP tube thicknesses are compared in Fig. 19. Hoop strain increases more slowly in general with the development of axial strain for the specimens with the thicker outer GFRP tube, due to the stronger confinement provided.

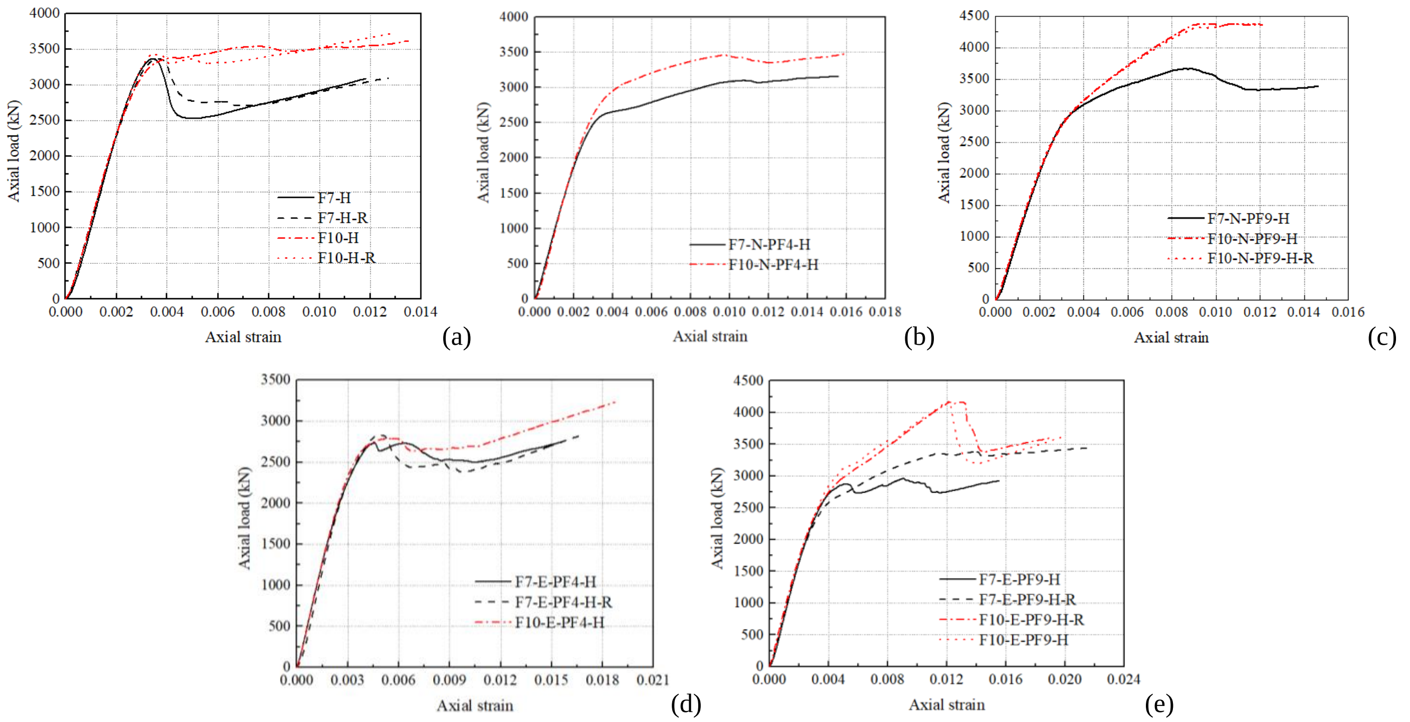

Fig. 18 Effect of outer filament winding GFRP tube on axial load-axial strain curves

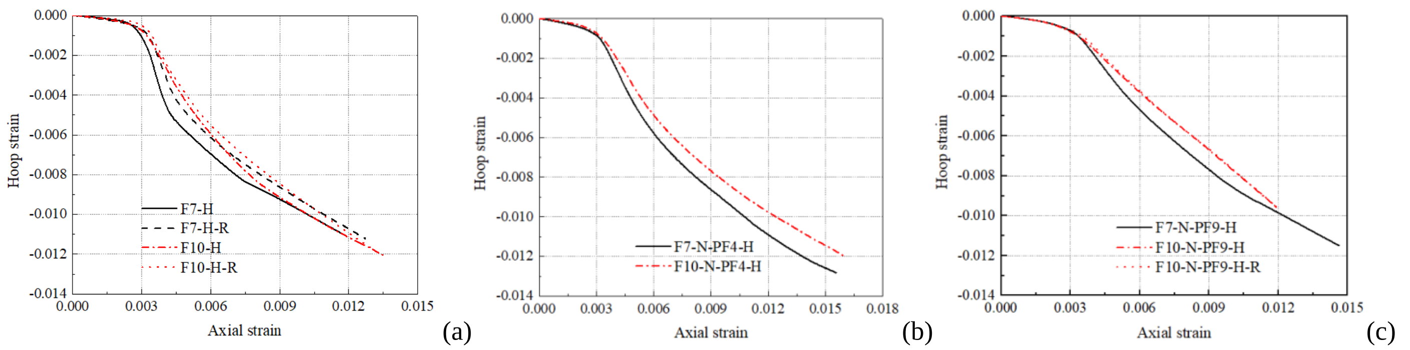

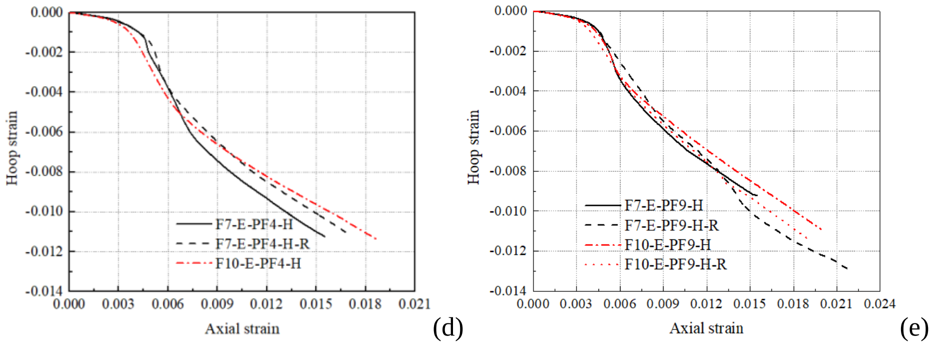

Fig. 19 Effect of outer filament winding GFRP tube on hoop strain-axial strain curves

4.3.2 Pultruded GFRP tube thickness

As shown in Fig. 11(k), the bearing capacity of PF9 is significantly higher than that of PF4. Therefore, it can be observed in Fig. 20 that at the first strain hardening stage, both the stiffness and the compressive load of the GFRP-concrete double tube composite columns with PF9 as inner tube are improved compared with those of the double tube composite columns with PF4 as inner tube. It is also worth noting that the improvements are more obvious for the specimens with F10 as outer GFRP tube as shown in Figs. 20(c) and (d). Meanwhile, the thicker inner pultruded GFRP tube will not only lead to the more uniform hoop strain distribution as presented in Fig. 16, but also restrain the increase of hoop strain. Much slower hoop strain growth can be observed, as shown in Fig. 21, for the specimens with FP9 as inner tube in comparison to those with PF4 as inner tube.

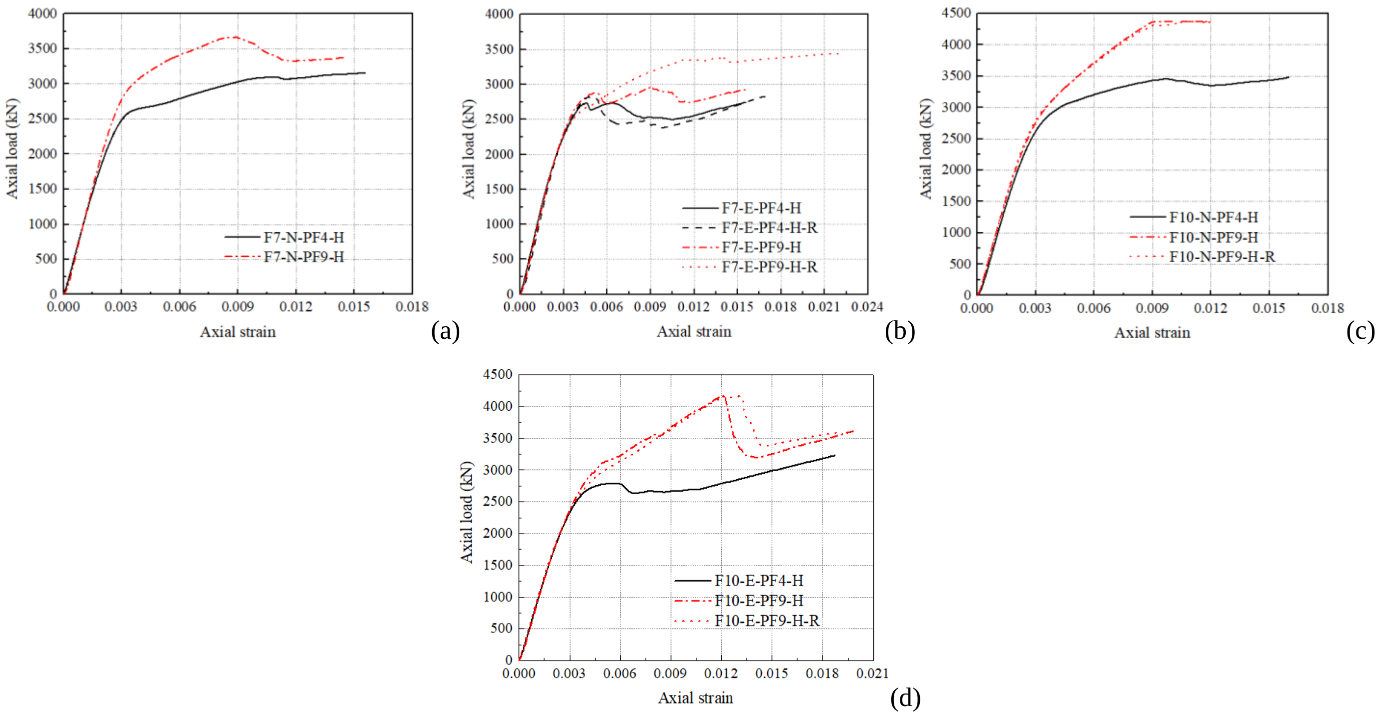

Fig. 20 Effect of inner pultruded GFRP tube on axial load-axial strain curves

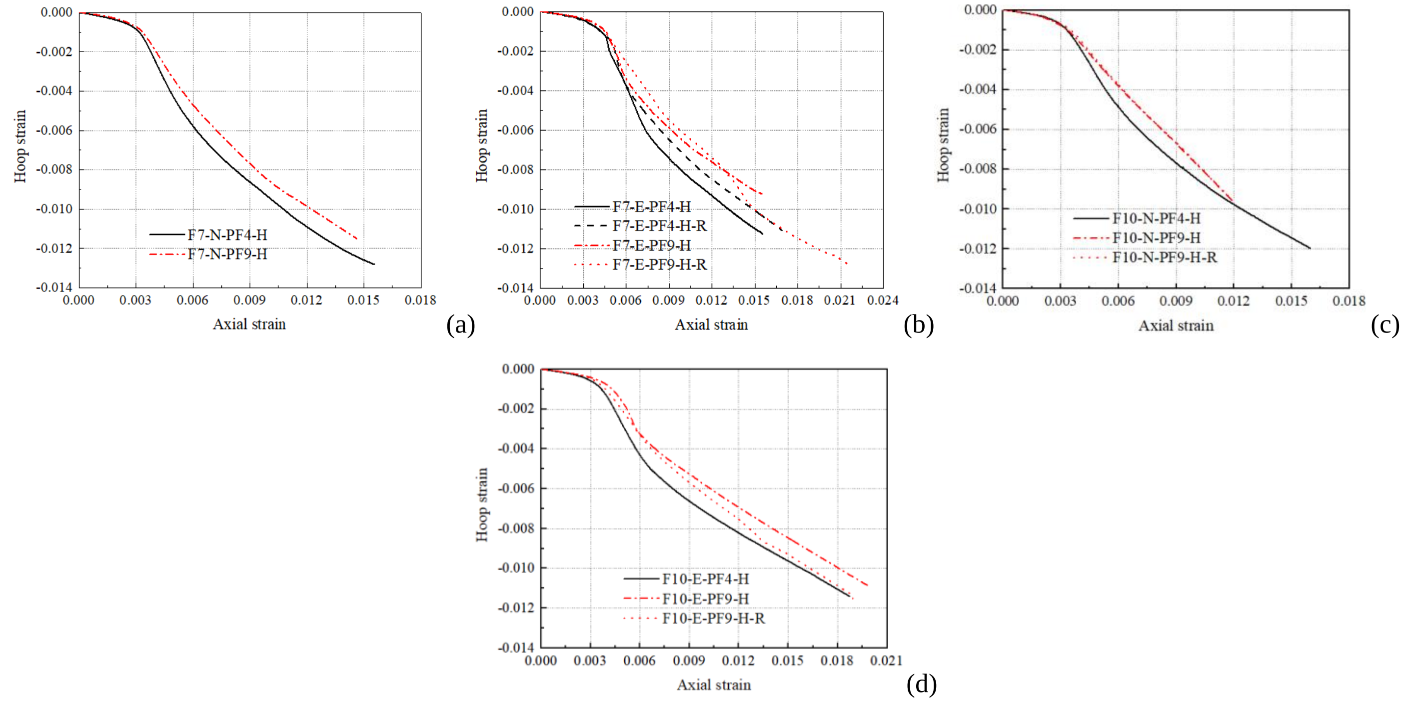

Fig. 21 Effect of inner pultruded GFRP tube on hoop strain-axial strain curves

4.3.3 Ring concrete

Figs. 22 and 23 present the comparisons of GFRP-concrete double tube composite columns with NC and ECC as ring concrete. Due to the lower compressive strength and elastic modulus of ECC than those of NC, both the initial stiffness and compressive load capacity of the specimens with ECC as ring concrete are lower in comparison to those of specimens with NC as ring concrete. It is known that the dilation of ECC under compression is at a lower level than NC. Therefore, the hoop strain increases obviously more slowly for the specimens with ECC as ring concrete. The ultimate axial strain is generally improved when ECC ring is adopted, indicating the improved deformability of the composite column.

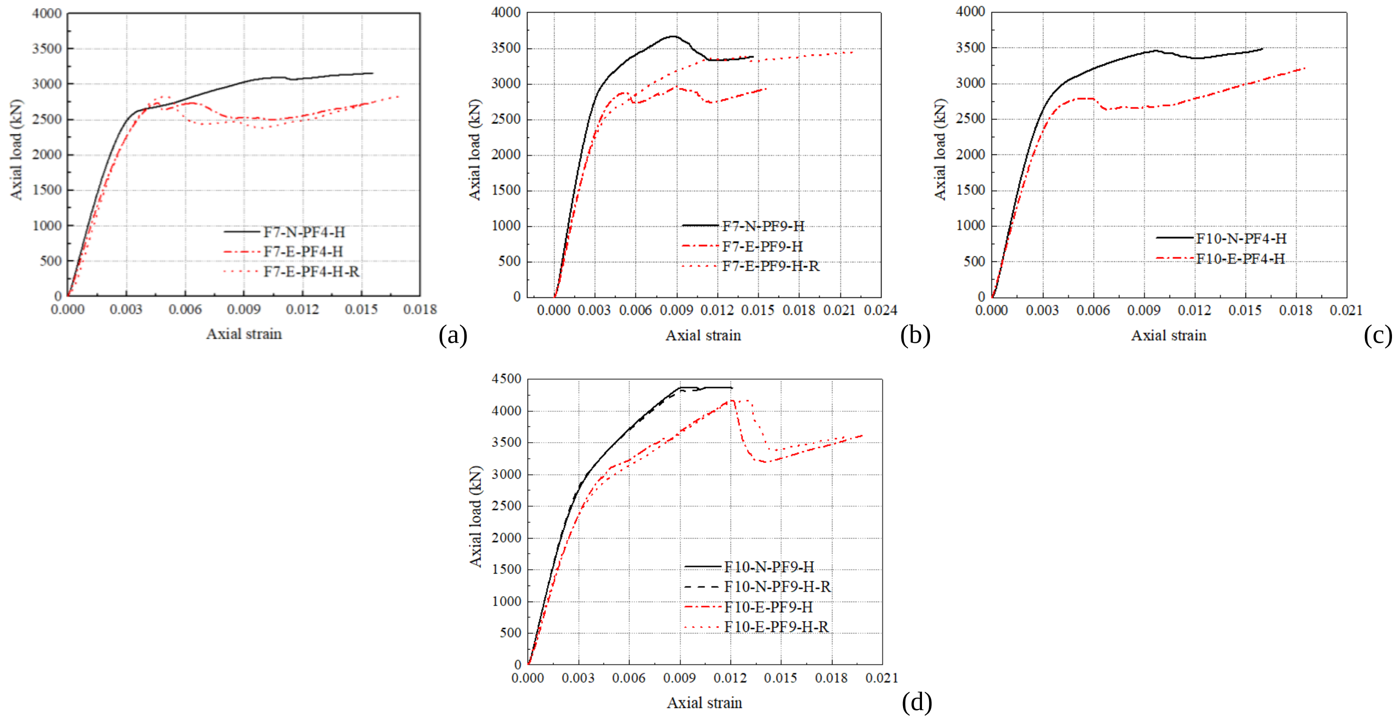

Fig. 22 Effect of ring concrete on axial load-axial strain curves

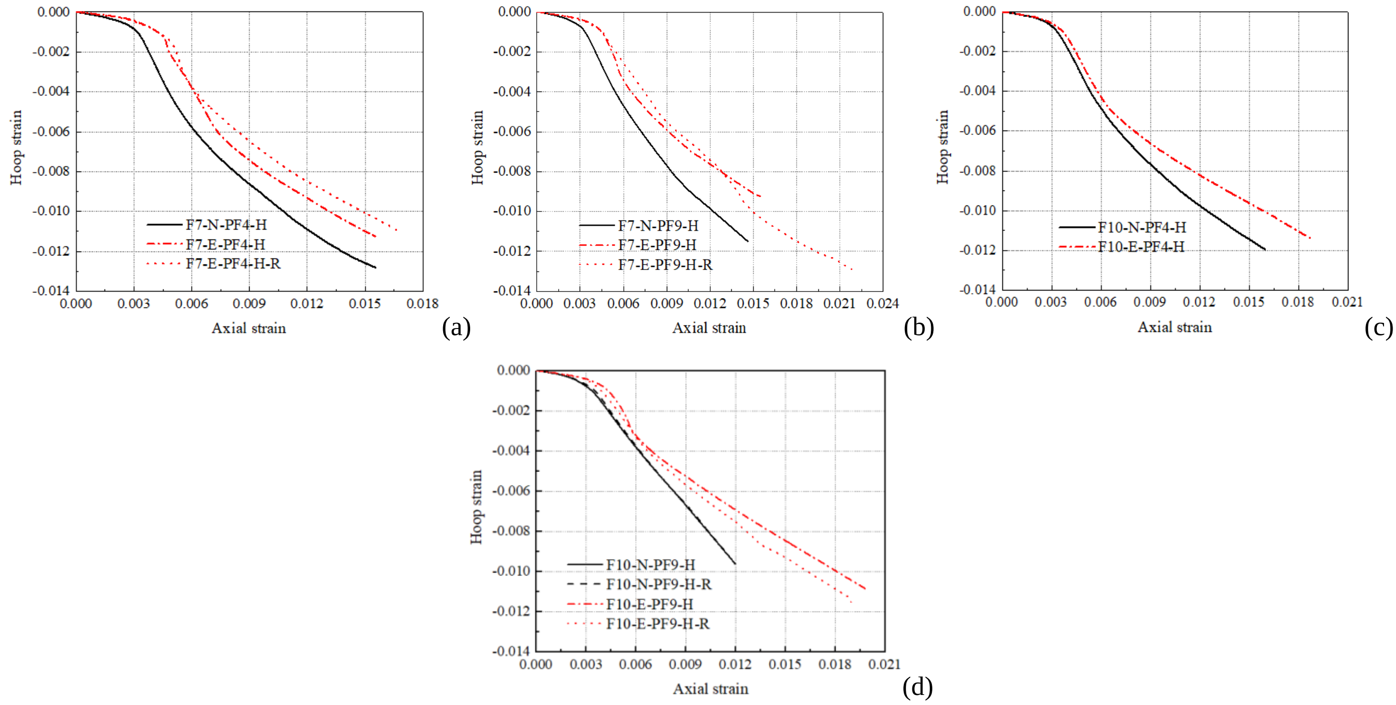

Fig. 23 Effect of ring concrete on hoop strain-axial strain curves

5. Predictions of ultimate conditions

5.1 Ultimate load carrying capacity

Compared with GFRP-confined HSC columns, the proposed GFRP-concrete double tube composite columns could generally develop similar or higher maximum load carrying capacity, except for the specimens F7-E-PF4-H(-R) and F10-E-PF4-H which have ECC ring of relatively lower compressive strength and thinner inner pultruded GFRP tube PF4. Analysis of load carrying capacity of GFRP-concrete double tube composite columns could be more complicated in comparison to the normal GFRP-confined HSC columns, because of the presence of inner tube and two types of concrete involved. Fig. 24 shows the mechanical diagram of different components in the double tube composite column. A_{core}, A_{ring}, A_{PF} and A_F are representing the sectional areas of core concrete, ring concrete, inner pultruded GFRP tube and outer filament winding GFRP tube, respectively. $f_{l,core}$ is the confining pressure applied on the core concrete, while $f_{li,ring}$ and $f_{lo,ring}$ are the confining pressures applied on inner side and outer side of the ring concrete.

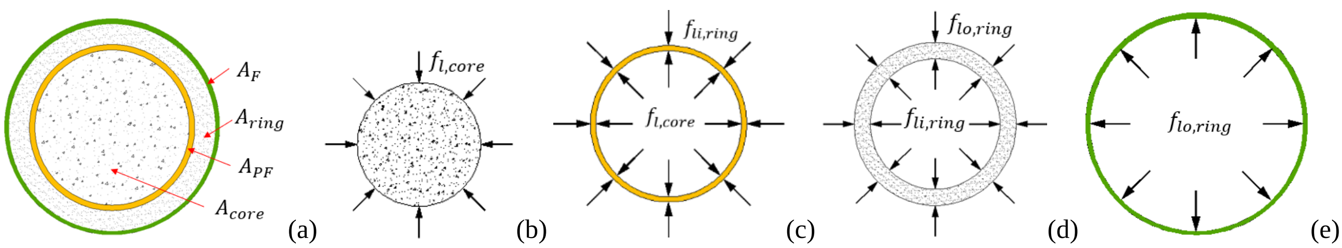

Fig. 24 Mechanical diagram of GFRP-concrete double tube composite column: (a) cross section; (b) core concrete; (c) inner pultruded GFRP tube; (d) ring concrete; (e) outer filament winding GFRP tube

Load carrying capacity of GFRP-concrete double tube composite column can be calculated by the superposition of the load capacity of different components, as shown in the following expression:

$$F = A_{core}f_{core} + A_{ring}f_{ring} + A_F f_F + A_{PF} f_{PF} \quad (1)$$

in which f_{core} and f_{ring} are the confined concrete strengths of core concrete and ring concrete; f_F and f_{PF} are the axial compressive strengths of outer filament winding GFRP tube and inner pultruded GFRP tube.

Due to the different types of concrete adopted in the core and ring regions in the composite column, the core concrete of solid circular section is under uniform confinement, while the ring concrete of annular section is under non-uniform confinement. However, it is considered that the confining pressures are not much different between the core concrete and ring concrete, since they are both concrete materials with similar compressive behavior. In the elastic stage, it is believed that the concrete and the GFRP tubes are in good contact, since the Poisson's ratio of the outer tube is lower than that of the ring concrete and the inner tube is embedded between core concrete and ring concrete. In the post-elastic stage when concrete cracks significantly, the lateral dilation becomes relatively large. Both the inner and outer GFRP tubes could keep the good contact with the concrete. Meanwhile, it is considered that the confinement effect is provided by the outer filament winding GFRP tube only in the composite column. Since the hoop stiffness is quite low due to the absence of fiber in the hoop direction for the inner pultruded GFRP tube, it cannot provide additional confinement to the core concrete. The hoop tensile strength of ECC ring is negligible in comparison to that of the outer GFRP tube. It will not contribute to the confinement effect as well. Therefore, it is assumed that the confining pressures applied on the core concrete and ring concrete are the same and both equal to that provided by the outer filament winding GFRP tube. The confining pressure f_l can be calculated as follows:

$$f_l = f_{l,core} = f_{li,ring} = f_{lo,ring} = K_l \varepsilon_h = \frac{2E_f t_f \varepsilon_h}{D} \quad (2)$$

where E_f, t_f, D and ε_h are the elastic modulus, thickness, inner diameter and hoop strain of the outer filament winding GFRP tube; K_l is the confining stiffness. For the ultimate condition at GFRP rupture, the corresponding confining pressure f_{lu} is expressed as:

$$f_{lu} = K_l \varepsilon_{h,rup} \quad (3)$$

in which $\varepsilon_{h,rup}$ is the actual hoop rupture strain of the outer filament winding GFRP tube.

Lam and Teng [54] developed design-oriented model for FRP-confined concrete, which could directly predict the stress-strain behavior and has also been adopted by the UK Concrete Society [55] and ACI 440.2R-17 [56] with some modifications. Teng et al. [57] subsequently proposed more accurate equations to predict the ultimate conditions in the design-oriented model, including ultimate compressive strength and ultimate axial strain. The ultimate compressive strength f'_{cc} can be expressed as follows:

$$f'_{cc} = f'_{c0} + k_1(\rho_K - a)\rho_\varepsilon f'_{c0} \quad (4)$$

$$\rho_K = \frac{K_l}{f'_{c0}/\varepsilon_{c0}} = \frac{2E_f t_f}{\left(f'_{c0}/\varepsilon_{c0}\right)D} \tag{5}$$

$$\rho_\varepsilon = \frac{\varepsilon_{h,rup}}{\varepsilon_{c0}} \tag{6}$$

in which f'_{c0} and ε_{c0} are compressive strength and the corresponding compressive strain of unconfined concrete; ρ_K is confinement stiffness ratio and represents the stiffness of confining FRP relative to that of the confined concrete; ρ_ε is the strain ratio reflecting the strain capacity of confining FRP; k_1 is the strength enhancement coefficient and a is the confinement stiffness ratio threshold for effective confinement. The term $(\rho_K - a)$ can be understood as the actual effective confinement stiffness ratio. It is regressed by Teng et al. [57] that $k_1 = 3.5$ and $a = 0.01$ based on the test database with the concrete strength ranging from 33.1 to 47.6 MPa. However, Eq. (4) with this set of values would provide much higher predictions on the ultimate compressive strength for the GFRP-confined HSC columns F7-H(-R) and F10-H(-R) investigated in this study. It is widely accepted that with the increase of concrete strength, the increased brittleness would decrease the confinement effect providing the same FRP confining material used [58-61]. Hence, a larger confinement stiffness ratio threshold could be considered for GFRP-confined HSC. To best-fit the test results of the tested specimens F7-H(-R) and F10-H(-R), $a = 0.035$ was adopted in Eq. (4) for the ultimate compressive strength prediction, while $k_1 = 3.5$ was remained unchanged to assume that the same strength enhancement effect could be obtained after reaching the effective confinement. If Eq. (4) with the modified parameter can provide accurate predictions on the ultimate compressive strength of GFRP-confined HSC column, it is believed that it can also provide close predictions on the ultimate compressive strength for the confined HSC core in the GFRP-concrete double tube composite column. Therefore, the confined concrete strength for core concrete f_{core} in Eq. (1) corresponding to the ultimate FRP rupture can be expressed as:

$$f_{core} = f'_{cc,HSC} = f'_{c0,HSC} + 3.5(\rho_K - 0.035)\rho_\varepsilon f'_{c0,HSC} \tag{7}$$

For double tube composite columns with NC as the ring concrete, the compressive strength of unconfined NC is 63.2 MPa. Meanwhile, relatively uniform cracking, rather than localized cracking like HSC core, was observed for the failed specimens. Therefore, Eq. (4) with the original confinement stiffness ratio threshold $a = 0.01$ was adopted to predict the ultimate compressive strength of NC ring concrete f_{ring} as follows:

$$f_{ring} = f'_{cc,NC} = f'_{c0,NC} + 3.5(\rho_K - 0.01)\rho_\varepsilon f'_{c0,NC} \tag{8}$$

For FRP-confined ECC, the stress-strain behavior could be different from that of FRP-confined normal concrete. The existing research on FRP-confined ECC is still limited in the current stage. Li et al. [62] experimentally investigated the behavior of ECC under a series of confining pressures and developed equations to describe the compressive strength and the corresponding compressive strain of ECC with respect to certain confining pressure. Dang et al. [63] conducted monotonic and cyclic axial compression tests on FRP-confined ECC and proposed predictions on the ultimate conditions including both compressive strength and strain. Yuan et al. [64] observed that the dilation behavior of FRP-confined ECC was different from that of FRP-confined normal concrete. The development of hoop strain is more restricted due to the self-confinement effect of ECC. A new equation was also proposed to express the hoop strain-axial strain behavior based on the test results. In this current study, the following Eq. (9), proposed by Dang et al. [63], was adopted to predict the ultimate compressive strength of ECC ring concrete f_{ring}:

$$f_{ring} = f'_{cc,ECC} = f'_{c0,ECC} + 2.5f_{lu} \tag{9}$$

where f_{lu} is the confining pressure at FRP rupture and can be calculated by Eq. (3).

In Eq. (1), the compressive strengths of outer filament winding GFRP tube and inner pultruded GFRP tube at GFRP rupture are also needed to be determined for obtaining the ultimate load carrying capacity of the GFRP-concrete double tube composite column. The ultimate compressive strain of hollow outer filament winding GFRP tube is lower than the ultimate axial compressive strain of the composite column. Since the outer GFRP tube is fully supported by the inner concrete, the axial buckling failure is believed to be delayed and the axial load carrying capacity will not lose immediately. Therefore, the compressive strength f_F is assumed to be unchanged when reaching the ultimate compressive strain till GFRP rupture. Meanwhile, the load carried by the outer filament winding GFRP tube is quite limited compared with that carried by the inner concrete. No significant effect would be caused with this assumption.

The failure of inner pultruded GFRP tube occurred before the GFRP rupture of the outer tube. As discussed in section 4.1, load contributed by the pultruded GFRP tube will not lose completely because the pultruded GFRP tube is embedded in concrete and the failure is restrained. The load drop from point B to point C in Fig. 15, which is also the difference between the load F_1 and F_2 as presented in Table 5, is around 30% of the load carrying capacity of the corresponding hollow pultruded GFRP tube for all the tested GFRP-concrete double tube composite columns on average. To be conservative, 50% load reduction is considered when pultruded GFRP tube reaches the compressive strain, leading to the residual load carrying capacity of the inner tube equals to 50% of the maximum load carrying capacity of the corresponding hollow pultruded GFRP tubes. Fig. 25 shows the axial load-axial strain behavior of outer filament winding GFRP tube and inner pultruded GFRP tube adopted for the load carrying capacity prediction of GFRP-concrete double tube composite columns. It is noted that in Fig. 25, the curves for PF4 and PF9 are determined based on the compression test results on hollow pultruded GFRP tubes, while the curves for F7 and F10 are calculated according to the stress-strain curves of compressive material tests on GFRP rings with the use of corresponding sectional areas of outer filament winding GFRP tube.

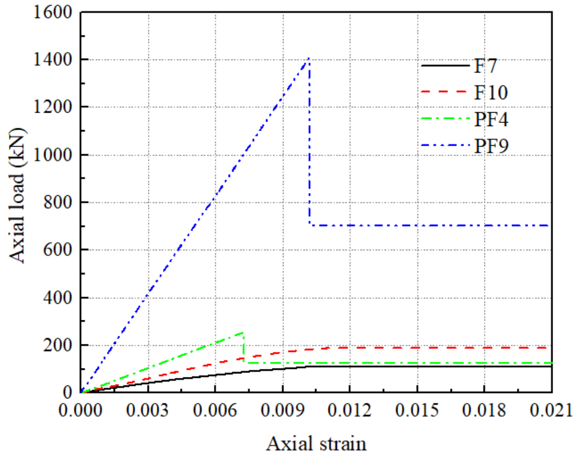

Fig. 25 Axial load-strain behavior adopted for GFRP tubes in load carrying capacity predictions

With the compressive strengths for different components determined as above, the ultimate load carrying capacity of the GFRP-concrete double tube composite column could be calculated with Eq. (1). Comparisons of the ultimate load carrying capacity between test results $F_{c,test}$ and prediction results $F_{c,pred}$ are shown in Table 6 and Fig. 26(a). Close agreements can be achieved with the mean value of 1.00 and coefficient of variation (Cov) value of 0.031. It demonstrates that the proposed equations could provide good predictions on the ultimate load carrying capacity for the tested composite columns.

Table 6 Ultimate conditions by tests and predictions

Specimen label	Ultimate load carrying capacity			Ultimate axial strain		
	$F_{c,test}$ (kN)	$F_{c,pred}$ (kN)	$F_{c,test}/F_{c,pred}$	$\varepsilon_{cu,test}$	$\varepsilon_{cu,pred}$	$\varepsilon_{cu,test}/\varepsilon_{cu,pred}$
F7-N-PF4-H	3156.9	3043.5	1.04	0.0156	0.0132	1.19
F7-N-PF9-H	3385.5	3375.7	1.00	0.0146	0.0129	1.13
F7-E-PF4-H	2746.3	2860.7	0.96	0.0155	0.0186	0.83
F7-E-PF4-H-R	2827.4	2854.4	0.99	0.0169	0.0185	0.91
F7-E-PF9-H	2925.2	3169.4	0.92	0.0155	0.0178	0.87
F7-E-PF9-H-R	3442.5	3287.8	1.05	0.0218	0.0192	1.13
F10-N-PF4-H	3481.0	3531.3	0.99	0.0160	0.0139	1.15
F10-N-PF9-H*	4371.0	4253.7	1.03	-	-	-
F10-N-PF9-H-R*	4370.0	4314.7	1.01	-	-	-
F10-E-PF4-H	3229.3	3301.5	0.98	0.0187	0.0199	0.94
F10-E-PF9-H	3619.9	3616.7	1.00	0.0199	0.0198	1.00
F10-E-PF9-H-R	3592.8	3653.3	0.98	0.0189	0.0201	0.94
F7-H	3086.6	3043.8	1.01	0.0118	0.0122	0.96
F7-H-R	3093.7	3042.8	1.02	0.0127	0.0123	1.03
F10-H	3613.7	3584.1	1.01	0.0135	0.0134	1.01
F10-H-R	3729.7	3570.5	1.04	0.0130	0.0133	0.98
Mean			1.00			1.01
Cov			0.031			0.105

*Note: For specimens F10-N-PF9-H(-R), the ultimate load carrying capacity is referring to the maximum axial load recorded in tests.

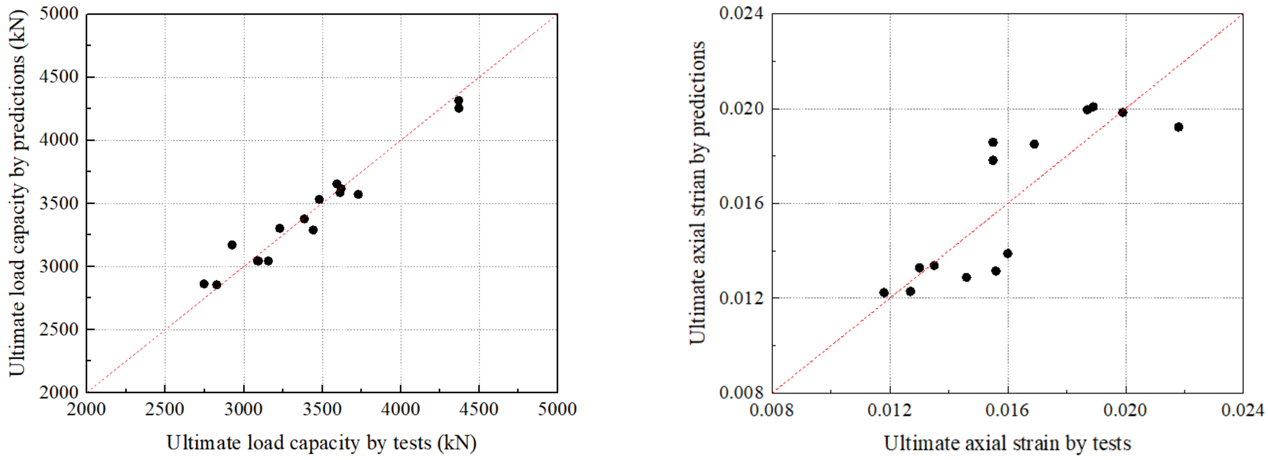

(a) Ultimate load carrying capacity (b) Ultimate axial strain

Fig. 26 Comparisons between test results and prediction results

5.2 Ultimate axial strain

Ultimate axial strains of the tested specimens are summarized and compared in Fig. 27. All of the proposed GFRP-concrete double tube composite columns present improved ultimate axial strain in comparison to the corresponding GFRP-confined HSC columns, except for the specimens F10-N-PF9-H(-R) which were not loaded to failure due to the limited machine capacity. The improvements are 19.2-52.2% and 20.8-46.4% for specimens with F7 and F10 as the outer filament winding GFRP tube, respectively. It is also worth noting that by comparing with F7-H(-R) and F10-H(-R) as well as F7-H(-R) and the double tube composited columns with F7 as the outer GFRP tube, the proposed GFRP-concrete double tube composite columns are more effective to reach a larger ultimate axial strain and deformability than increasing the outer confining GFRP tube thickness from F7 to F10.

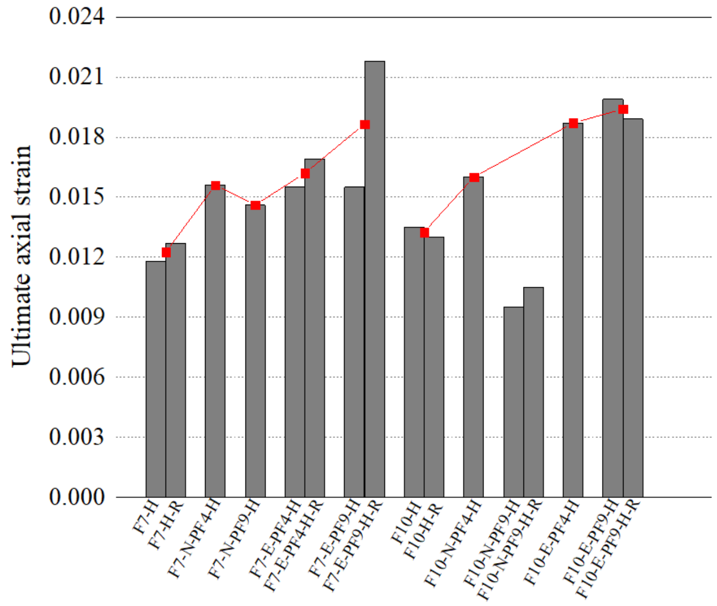

Fig. 27 Comparison of ultimate axial strain for tested specimens

Many design equations have been developed to predict the ultimate axial strain for FRP-confined concrete [57,65-68]. Most of them adopt the form proposed by Teng et al. [57], as shown in the following Eq. (10), relating the ultimate axial strain to the confinement stiffness ratio and strain ratio.

$$\frac{\varepsilon_{cu}}{\varepsilon_{c0}} = C + k_2 f(\rho_K) g(\rho_\varepsilon) \tag{10}$$

in which C is constant; k_2 is strain enhancement coefficient; $f(\rho_K)$ and $g(\rho_\varepsilon)$ are functions of the confinement stiffness ratio and the strain ratio. The constant C is taken as 1.75 by Teng et al. [57], so that it can yield $\varepsilon_{cu} = 0.0035$ when $\varepsilon_{c0} = 0.002$ for concrete with no FRP confinement. 0.002 is generally adopted as the strain at unconfined compressive strength of normal strength concrete, while 0.0035 is the corresponding ultimate compressive strain. However, it is mentioned that the constant 1.75 can be adjusted to suit the specific case of unconfined concrete with the different values of ε_{c0} and ε_{cu} [57]. For unconfined high strength concrete, the compressive failure is brittle and the ultimate compressive strain ε_{cu} is normally the same as the strain ε_{c0} corresponding to the compressive strength f'_{c0}. Therefore, $C = 1$ is adopted in this study for conservative predictions of the ultimate compressive strain of the composite columns with high strength concrete. For simplicity, Eq. (10) is rewritten as follows:

$$\frac{\varepsilon_{cu}}{\varepsilon_{c0}} = 1 + k_2 (\rho_K \rho_\varepsilon)^b = 1 + k_2 (\frac{f_{lu}}{f'_{c0}})^b \tag{11}$$

in which the ultimate axial strain is directly related to the confining pressure f_{lu}. This simplified form has equivalently considered the effect of confinement stiffness ratio and strain ratio and has been adopted in the existing design-oriented models for FRP-confined concrete [68,69]. It is found that the strain enhancement coefficient $k_2 = 5.4$ and the index $b = 0.3$ could best-fit the test results of F7-H(R) and F10-H(R). For the prediction of GFRP-concrete double tube composite columns, $f'_{c0,ave}$, which is the average unconfined strength of core concrete $f'_{c0,core}$ and ring concrete $f'_{c0,ring}$, is adopted and can be calculated as:

$$f'_{c0,ave} = (f'_{c0,core} A_{core} + f'_{c0,ring} A_{ring}) \Big/ (A_{core} + A_{ring}) \tag{12}$$

Meanwhile, the larger axial strain $\varepsilon_{c0,lrg}$ between core concrete and ring concrete is used to consider the benefit brought to the ultimate axial strain of double tube composite columns to the utmost extent. Therefore, the following Eq. (13) is generated to predict the ultimate axial strain ε_{cu} of GFRP-concrete double tube composite columns:

$$\varepsilon_{cu} = \varepsilon_{c0,lrg} + 5.4 (\frac{f_{lu}}{f'_{c0,ave}})^{0.3} \varepsilon_{c0,lrg} \tag{13}$$

Prediction results $\varepsilon_{cu,pred}$ are summarized in Table 6 and compared with test results $\varepsilon_{cu,test}$ in Fig. 26(b). Close agreements with the mean value of 1.01 and coefficient of variation (Cov) value of 0.105 indicate the promising predictions on the ultimate axial strain of the tested specimens.

It should be noted that the actual GFRP rupture strain of each tested specimen is used for the validation purpose for both ultimate load carrying capacity and ultimate axial strain. For design purpose, FRP material rupture strain after considering the strain efficiency factor [52,69-72] can be adopted for the calculation.

6. Conclusions

A novel GFRP-concrete double tube composite column was proposed and studied through axial compression tests. Effects of different parameters, including outer filament winding GFRP tube thickness, inner pultruded GFRP tube thickness and ring concrete material, were investigated and examined. Compared with corresponding normal GFRP-confined HSC columns, the proposed GFRP-concrete double tube composite columns exhibit superior compressive behavior. The following conclusions can be drawn within the current scope of this study:

(1) Failure of all the tested specimens is governed by outer filament winding GFRP tube rupture in the hoop direction. Inner pultruded GFRP tube in the GFRP-concrete double tube composite column failed prior to the outer GFRP tube rupture, then followed by a load drop. The load carrying capacity would still recover to withstand a new strain hardening stage until rupture of the outer GFRP tube.

(2) Load carrying capacity of the double tube composite column is increased with the increase of outer filament winding GFRP tube thickness from 2.5 mm (F7) to 3.5 mm (F10) as well as the inner pultruded GFRP tube thickness from 4.0 mm (PF4) to 9.0 mm (PF9). Compared with specimens with NC as ring concrete, the specimens with ECC as ring concrete would develop a relatively lower load carrying capacity due to the lower compressive strength of ECC than that of NC.

(3) The proposed GFRP-concrete double tube composite column could develop more uniform hoop strain distribution in comparison to the corresponding GFRP-confined HSC column. It is also noted that the hoop strain would be more uniformly distributed if thicker inner pultruded GFRP tube as well as ECC ring are adopted for the double tube composite column.

(4) Compared with the GFRP-confined HSC columns, the GFRP-concrete double tube composite column has a lower hoop strain at the same axial strain and presents a slower development with the increase of axial strain. This effect is more obvious when thicker inner pultruded GFRP tube and ECC ring are used for the double tube composite column.

(5) Compared with GFRP-confined HSC column, the ultimate axial strain of GFRP-concrete double tube composite column is improved by 19.2-52.2% and 20.8-46.4% for specimens with F7 and F10 as the outer filament winding GFRP tube, respectively. The improvement is more significant for columns adopting ECC as the ring concrete. It demonstrates that the proposed composite column is effective to achieve an enhanced deformability.

(6) Design equations for predicting the ultimate load carrying capacity and ultimate axial strain of the GFRP-concrete double tube composite column are proposed and verified against the test results obtained from this study. The close agreements between prediction results and test results reveal the promising performance of the proposed equations within the current scope of the study.

It is worth noting that the ratio of the inner tube diameter to the outer tube diameter could have influence on the column performance. Further experimental and numerical investigations will be carried out to achieve a more comprehensive understanding and provide design guidelines for the GFRP-concrete double tube composite columns.

CRediT authorship contribution statement

Shuai Li: Investigation, Writing - original draft. **Tak-Ming Chan:** Writing - review & editing, Funding acquisition, Supervision. **Ben Young:** Writing - review & editing, Funding acquisition, Supervision.

Declaration of Competing Interest

The authors declare that they have no known competing financial interests or personal relationships that could have appeared to influence the work reported in this paper.

Acknowledgement

The research work presented in this paper was supported by the Research Grants Council of the Hong Kong Special Administrative Region, China – Theme-based Research Scheme (Project No. T22-502/18-R).

References

[1] H. Fang, T.-M. Chan, B. Young, Structural performance of concrete-filled cold-formed high-strength steel octagonal tubular stub columns, Eng. Struct. 239 (2021) 112360.

[2] Y.C. Cai, W.M. Qucah, B. Young, Experimental and numerical investigation of concrete-filled hot-finished and cold-formed steel elliptical tubular stub columns, Thin-Walled Struct. 145 (2019) 106437.

[3] J.Y. Zhu, J. Chen, T.-M. Chan, Analytical model for circular high strength concrete filled steel tubes under compression, Eng. Struct. 244 (2021) 112720.

[4] J. Chen, T.-M. Chan, Compressive behaviour and design of compact to slender octagonal concrete-filled steel tubular stub columns, Thin-Walled Struct. 167 (2021) 108211.

[5] Y.L. Li, J.G. Teng, X.L. Zhao, R.K. Singh Raman, Theoretical model for seawater and sea sand concrete-filled circular FRP tubular stub columns under axial compression, Thin-Walled Struct. 160 (2018) 71-84.

[6] Y.L. Li, X.L. Zhao, R.K. Singh Raman, S. Al-Saadi, Experimental study on seawater and sea sand concrete filled GFRP and stainless steel tubular stub columns, Thin-Walled Struct. 106 (2016) 390-406.

[7] L.H. Han, C.-Y. Xu, Z. Tao, Performance of concrete filled stainless steel tubular (CFSST) columns and joints: summary of recent research, J. Constr. Steel Res. 152 (2019) 117–131.

[8] Z.H. Chen, S.H. Dong, Y.S. Du, Experimental study and numerical analysis on seismic performance of FRP confined high-strength rectangular concrete-filled steel tube columns, Thin-Walled Struct. 162 (2021)107560.

[9] J. Xie, Z. Wang, J.B. Yan, Axial compression behaviours of seawater and sea sand concrete-filled GFRP stub tubes at arctic low temperatures, Thin-Walled Struct, 170 (2022) 108566.

[10] T. Ozbakkaloglu, J.C. Lim, T. Vincent, FRP-confined concrete in circular sections: Review and assessment of stress–strain models, Eng. Struct. 49 (2013) 1068–1088.

[11] M.H. Lai, Y.W. Liang, Q. Wang, F.M. Ren, M.T. Chen, J.C.M. Ho, A stress-path dependent stress-strain model for FRP-confined concrete, Eng. Struct. 203 (2020) 109824.

[12] M.H. Lai, W. Song, X.L. Ou, M.T. Chen, Q. Wang, J.C.M. Ho, A path dependent stress-strain model for concrete-filled-steel-tube column, Eng. Struct. 211 (2020) 110312.

[13] J.C.M. Ho, X.L Ou, M.T. Chen, Q. Wang, M.H. Lai, A path dependent constitutive model for CFFT column, Eng. Struct. 210 (2020) 110367.

[14] J.G. Teng, T. Yu, Y.L. Wong, S.L. Dong, Hybrid FRP–concrete–steel tubular columns: Concept and behavior, Construct. Build. Mater. 21 (2007) 846-854.

[15] T. Yu, B. Zhang, Y.B. Cao, J.G. Teng, Behavior of hybrid FRP-concrete-steel double-skin tubular columns subjected to cyclic axial compression, Thin-Walled Struct. 61 (2012) 196-103.

[16] B. Zhang, T. Yu, J.G. Teng, Behavior and modelling of FRP-concrete-steel hybrid double-skin tubular columns under repeated unloading/reloading cycles, Compos. Struct. 258 (2021) 113393.

[17] Z.L. Chen, J. Wang, J.Y. Chen, H. GangaRao, R.F. Liang, W.Q. Liu, Responses of concrete-filled FRP tubular and concrete-filled FRP-steel double skin tubular columns under horizontal impact, Thin-Walled Struct. 155 (2020) 106941.

[18] J.J. Zeng, Y.Z. Zheng, Y.L. Long, Axial compressive behavior of FRP-concrete-steel double skin tubular columns with a rib-stiffened Q690 steel tube and ultra-high strength concrete, Compos. Struct. 268 (2021) 113912.

[19] Y.L. Li, X.L. Zhao, Singh Raman, S. Al-Saadi, Tests on seawater and sea sand concrete-filled CFRP, BFRP and stainless steel tubular stub columns, Thin-Walled Struct. 108 (2016) 163-184.

[20] J.J. Zeng, S.D. Liang, Y Zhuge, J.K. Zhou, J.J. Liao, Seismic behavior of FRP-concrete-steel double skin tubular columns with a rib-stiffened Q690 steel tube and high-strength concrete, Thin-Walled Struct. 175 (2022) 109127.

[21] Y.L. Li, X.L. Zhao, Hybrid double tube sections utilising seawater and sea sand concrete, FRP and stainless steel, Thin-Walled Struct. 149 (2020) 106643.

[22] J.J. Zeng, J.F. Lv, G. Lin, Y.C. Guo, L.J. Li, Compressive behavior of double-tube concrete columns with an outer square FRP tube and an inner circular high-strength steel tube, Construct. Build. Mater. 184 (2018) 668-680.

[23] Y.Y. Ye, D.H. Zhu, J.J. Zeng, G. Lin, W.Q. Wang, Rectangular double-tube concrete columns with an internal elliptical high-strength steel tube: Concept and behavior, Eng. Struct. 216 (2020) 110742.

[24] Y.C. Guo, Y.Y. Ye, G. Lin, J.F. Lv, Y.L. Bai, J.J. Zeng, Effective usage of high strength steel tubes: Axial compressive behavior of hybrid FRP-concrete-steel solid columns, Thin-Walled Struct. 154 (2020) 106796.

[25] Y.L. Long, W.T. Li, J.G. Dai, L. Gardner, Experimental study of concrete-filled CHS stub columns with inner FRP tubes, Thin-Walled Struct. 122 (2018) 606-621.

[26] P. Feng, S. Chen, Y. Bai, L.P. Ye, Mechanical behavior of concrete-filled square steel tube with FRP-confined concrete core subjected to axial compression, Compos. Struct. 123 (2015) 312-324.

[27] Z.Y. Zhu, I. Ahmad, A. Mirmiran, Seismic performance of concrete-filled FRP tube columns for bridge substructure, J. Bridge Eng. 11(3) (2006) 359-370.

[28] H.M. Mohamed, M.Z. Afifi, B. Benmokrane, Performance evaluation of concrete columns reinforced longitudinally with FRP bars and confined with FRP hoops and spirals under axial load, J. Bridge Eng. 19(7) (2014) 04014020.

[29] J.G. Teng, T. Yu, J.G. Dai, G.M. Chen, FRP composites in new construction: current status and opportunities, In Proceedings of the 7th National Conference on FRP Composition. in Infrastructure (Supplementary Issue of Industrial Construction) (Abstract) Hangzhou, China (2011).

[30] J.K. Zhou, W.K. Lin, S.X. Guo, J.J. Zeng, Y.L. Bai, Behavior of FRP-confined FRP spiral reinforced concrete square columns (FCFRCs) under axial compression, J. Build. Eng. 45 (2022) 103452.

[31] J.G. Teng, B. Zhang, S.S. Zhang, B. Fu, Steel-free hybrid reinforcing bars for concrete structures, Adv. Struct. Eng. 21(16) (2018) 2617-1622.

[32] J.J. Zeng, Y.Y. Ye, W.M. Quach, G. Lin, Y. Zhuge, J.K. Zhou, Compressive and transverse shear behaviour of novel FRP-UHPC hybrid bars, Compos. Struct. 281 (2022) 115001.

[33] J.G. Teng, Y. Xiang, T. Yu, Z. Fang, Development and mechanical behaviour of ultra-high-performance seawater sea-sand concrete, Adv. Struct. Eng. 22(14) (2019) 3100-3120.

[34] V.C. Li, S. Wang, C. Wu, Tensile strain-hardening behavior of polyvinyl alcohol engineered cementitious composite (PVA-ECC), ACI Mater. J. 98(6) (2001) 483-492.

[35] V.C. Li, On engineered cementitious composites (ECC) - A review of the material and its applications, J. Adv. Concr. Technol. 1(3) (2003) 215-230.

[36] L.Y. Xu, B.T. Huang, V.C. Li, J.G. Dai, High-strength high-ductility Engineered/Strain-Hardening Cementitious Composites (ECC/SHCC) incorporating geopolymer fine aggregates, Cement Concr. Compos. 125 (2022) 104296.

[37] B.T. Huang, J.Q. Wu, J. Yu, J.G. Dai, C.K.Y. Leung, High-Strength Seawater Sea-sand Engineered Cementitious Composites (SS-ECC): Mechanical Performance and Probabilistic Modeling, Cement Concr. Compos. 114 (2020) 103740.

[38] C.K. Lee, M.K.I. Khan, Y.X. Zhang, M.M. Rana, Compressive performance of ECC-concrete encased high strength steel composite columns, Eng. Struct. 213 (2020) 110567.

[39] M.K.I. Khan, M.M. Rana, Y.X. Zhang, C.K. Lee, Compressive behaviour of engineered cementitious composites and concrete encased steel composite columns, J. Constr. Steel Res. 167 (2020) 105967.

[40] C.L. Nguyen, C.K. Lee, Flexural behaviours of Engineered Cementitious Composites – High strength steel composite beams, Eng. Struct. 249 (2021) 113324.

[41] M.I. Kabir, C.K. Lee, M.M. Rana, Y.X. Zhang, Strength enhancement of high strength steel beams by engineered cementitious composites encasement, Eng. Struct. 207 (2020) 110288.

[42] Japan Society of Civil Engineers, Recommendations for design and construction of high performance fiber reinforced cement composites with multiple fine cracks (HPFRCC). Concrete Engineering Series 82, 2008.

[43] T. Ozbakkaloglu, T. Vincent, Influence of fiber orientation and specimen end condition on axial compressive behavior of FRP-confined concrete, Constr. Build. Mater. 47 (2013) 814-826.

[44] B. Zhang, X.M. Hu, Q. Zhao, T. Huang, N.Y. Zhang, Q.B. Zhang, Effect of fiber angles on normal and high-strength concrete-filled fiber-reinforced polymer tubes under monotonic axial compression, Adv. Struct. Eng. 23(5) (2020) 924-940.

[45] ASTM D2290-08, Standard test method for apparent hoop tensile strength of plastic or reinforced plastic pipe by split disk method, American Society for Testing and Materials, Philadelphia, USA, 2008.

[46] GB/T5350-2005, Fiber-reinforced thermosetting plastic composites pipe: Determination for longitudinal compressive properties, The Standards Press of China, 2005.

[47] ASTM D3039-17, Standard test method for tensile properties of polymer matrix composite materials, American Society for Testing and Materials, Philadelphia, USA, 2017.

[48] ASTM D695-15, Standard test method for compressive properties of rigid plastics, American Society for Testing and Materials, Philadelphia, USA, 2015.

[49] B. Zhang, T. Yu, J.G. Teng, Behavior of concrete-filled concrete tubes under cyclic axial compression, J. Compos. Constr. 19(3) (2015) 04014060.

[50] N. Sirach, S.T. Smith, T. Yu, A. Mostafa, Experimental study on the confinement of concrete cylinders with large rupture-strain FRP composites, J. Compos. Constr. 25(4) (2021) 04021026.

[51] J.C. Lim, T. Ozbakkaloglu, Hoop strains in FRP-confined concrete columns: Experimental investigations, Mater. Struct. 48(9) (2014) 2839-2854.

[52] S.T. Smith, S.J. Kim, H. Zhang, Behavior and effectiveness of FRP wrap in the confinement of large concrete cylinders, J. Compos. Constr. 14(5) (2010) 573-582.

[53] A.F. Pour, T. Ozbakkaloglu, T. Vincent, Axial compressive behavior of ultra-high-strength steel fiber-reinforced concrete-filled fiber reinforced polymer (FRP) tube columns, Compos. Struct. 266 (2021) 113777.

[54] L. Lam, J.G. Teng, Design-oriented stress-strain model for FRP-confined concrete, Constr. Build. Mater. 17(6) (2003) 471-489.

[55] Concrete Society, Design guidance for strengthening concrete structures with fibre composite materials, Technical Rep. No. 55, 3rd Ed., Crowthorne, Berkshire, U.K. 2012.

[56] American Concrete Institute ACI, Guide for the design and construction of externally bonded FRP systems for strengthening concrete structures, ACI-440 2R, Farmington Hills, Mich. 2017.

[57] J.G. Teng, T. Jiang, L. Lam, Y.Z. Luo, Refinement of a design-oriented stress–strain model for FRP-confined concrete, J. Compos. Constr. 13(4) (2009) 269-278.

[58] T. Ozbakkaloglu, Behavior of square and rectangular ultra high strength concrete-filled FRP tubes under axial compression, Compos. Part B 54 (2013) 97–111.

[59] D.S. Oliveira, V. Raiz, R. Carrazedo, Experimental study on normal-strength, high-strength and ultrahigh-strength concrete confined by carbon and glass FRP laminates. J. Compos. Constr. 23(1) (2019) 04018072.

[60] A.F. Pour, A. Gholampour, J. Zheng, T. Ozbakkaloglu, Behavior of FRP-confined high-strength concrete under eccentric compression: Tests on concrete-filled FRP tube columns, Compos. Struct. 220 (2019) 261-272.

[61] T. Vincent, T. Ozbakkaloglu, Influence of concrete strength and confinement method on axial compressive behavior of FRP confined high- and ultra high-strength concrete, Compos. Part B 50 (2013) 413-428.

[62] Y. Li, W. Wang, C. Wen, Experiment study on mechanical performance of ECC under conventional triaxial compression, Concrete 1 (2016) 59–63 (in Chinese).

[63] Z. Dang, P. Feng, J.Q. Yang, Q. Zhang. Axial compressive behavior of engineered cementitious composite confined by fiber-reinforced polymer, Compos. Struct. 243 (2020) 112191.

[64] W.Y. Yuan, Q. Han, Y.L. Bai, X.L. Du, Z.W. Yan, Compressive behavior and modelling of engineered cementitious composite (ECC) confined with LRS FRP and conventional FRP. Compos. Struct. 272 (2021) 114200.

[65] J.C. Lim, T. Ozbakkaloglu. Confinement model for FRP-confined high strength concrete, J. Compos. Constr. 18(4) (2014) 4013058.

[66] J.C. Lim, T. Ozbakkaloglu. Stress-strain model for normal and light-weight concretes under uniaxial and triaxial compression, Constr. Build. Mater. 71 (2014) 492–509.

[67] A.F. Pour, T. Ozbakkaloglu, T. Vincent, Simplified design-oriented axial stress-strain model for FRP-confined normal- and high-strength concrete, Eng. Struct. 175 (2018) 501-516.

[68] J.J. Liao, J.J. Zeng, Q.M. Gong, W.M. Quach, W.Y. Gao, L. Zhang, Design-oriented stress-strain model for FRP-confined ultra-high performance concrete (UHPC), Constr. Build. Mater. 318 (2022) 126200.

[69] J.J. Zeng, Y.Y. Ye, W.Y. Gao, S.T. Smith, Y.C. Guo, Stress-strain behavior of polyethylene terephthalate fiber-reinforced polymer-confined normal-, high- and ultra high-strength concrete, J. Build. Eng. 30 (2020) 101243.

[70] S. Pessiki, K.A. Harries, J.T. Kestner, R. Sause, J.M. Ricles, Axial behavior of reinforced concrete columns confined with FRP jackets, J. Compos. Constr. 5(4) (2001) 237-245.

[71] L. Lam, J.G. Teng, Ultimate condition of fiber reinforced polymer-confined concrete, J. Compos. Constr. 8(6) (2004) 539–548.

[72] Y.F. Wu, J.F. Jiang, Effective strain of FRP for confined circular concrete columns, Compos. Struct. 95 (2013) 479-491.